SHAPE OPTIMIZATION OF THIN-WALLED TUBES UNDER HIGH-VELOCITY
AXIAL AND TRANSVERSE IMPACT LOADINGS

by

Niyazi Tanlak

B.S., Mechanical Engineering, Yıldız Technical University, 2005

M.S., Mechanical Engineering, Boğaziçi University, 2008

Submitted to the Institute for Graduate Studies in

Science and Engineering in partial fulfillment of

the requirements for the degree of

Doctor of Philosophy

Graduate Program in FBE Program for which the Thesis is Submitted

Boğaziçi University

2014

SHAPE OPTIMIZATION OF THIN-WALLED TUBES UNDER HIGH-VELOCITY
AXIAL AND TRANSVERSE IMPACT LOADINGS

APPROVED BY:

Prof. Fazıl Önder SÖNMEZ   . . . .
(Thesis Supervisor)

Assist. Prof. C. Can AYDINER   . . . .

Assist. Prof. Sami And KILIÇ   . . . .

Assoc. Prof. Bülent EKİCİ   . . . .

Assoc. Prof. Çetin YILMAZ   . . . .

DATE OF APPROVAL: 05.09.2014

ACKNOWLEDGEMENTS

ABSTRACT

SHAPE OPTIMIZATION OF THIN-WALLED TUBES UNDER HIGH-VELOCITY AXIAL AND TRANSVERSE IMPACT LOADINGS

Thin-walled tubes are one of the most commonly used parts in structural applications. More specifically, they are used as passive safety measures in vehicles like bumper-beams and crash-boxes. They take loads either mainly in the axial direction or transverse direction. The objective of this study is to develop a design optimization methodology to maximize the crash-worthiness of such parts. The method is applied to obtain optimal shape designs of a bumper-beam and a crash-box. They are modeled under the loading conditions in standard EuroNCAP tests in which the vehicle hits a deformable barrier with 40% offset by 64 km/h speed. The crash event is simulated using explicit finite element method. A lumped parameter model is developed to account for the structural response of the main vehicle body by a parametric system identification method. The tubes are optimized by a hybrid search algorithm combining genetic algorithm and Nelder&Mead simplex search. The results indicate significant improvement in the crash-worthiness of the tubes.

ÖZET

EKSENEL VE YANAL ÇARPIŞMA YÜKLERİNE MARUZ İNCE CİDARLI YAPILARIN ŞEKİL ENİYİLEMESİ

İnce cidarlı borular yapısal uygulamalarda en çok kullanılan elemanlardandır. Daha spesifik bakıldığında, taşıtlarda pasif güvenlik sistemleri, örneğin tampon kirişi ve tampon kirişi braketi, olarak kullanılırlar. Bu parçalar, genel bir bakış açısından, üzerlerine gelen yükleri yanal ve eksenel yönde alırlar. Bu çalışmanın amacı bu parçaların çarpışma kabiliyetlerini azami hale getirilmesi için bir yöntem ortaya koymaktır. Bu method tampon kirişi ve tampon kirişi braketinin şekilsel eniyilemesi tasarım sürecine uygulanmıştır. Söz konusu parçalar taşıtın 64 km/h hızla %40 ının bir bariyere çarptığı durumu inceleyen EuroNCAP testi esas alınarak irdelenmiştir. Bu test Açık Sonlu Elemanlar metodu kullanılarak simule edilmiştir. Aracın tamamının simulasyonu yapılmaktansa, araç ana gövdesi basitleştirilmiş bir modele benzetilmiştir. Parçalar genetik algoritma ve Nelder&Mead algoritmalarının birleşiminden elde edilen melez bir algoritma vasıtası ile şekilleri eniyilenmiştir. Eniyileme sonucunda önemli ilerlemenin sağlandığı görülmüştür.

TABLE OF CONTENTS

LIST OF FIGURES

LIST OF TABLES

LIST OF SYMBOLS

B	Strain hardening coefficient
c_i	Damping coefficient
C	Strain rate parameter
d_c	Decay coefficient
D_i	Failure strain constants
E	Young's modulus
E_{acc}	Energy accumulation
E_{bar}	Energy accumulation of the barrier
E_{ben}	Benchmark energy accumulation
E_{vint}	Energy absorbed by the vehicle
E_{vke}	Final kinetic energy of the car
f_{obj}	Objective function
F_{max}	Maximum transmitted force
I	Area moment of inertia
k_i	Stiffness of the spring
K	Hourglass stiffness
L	Length of the beam
m	Mass of the design
$m^{'}$	Reduced mass
m_{ben}	Mass of the benchmark shape
M	Moment
n	Strain hardening coefficient exponent
n_i	Normalization constants
p	Hydrostatic tension
P	Penalty function
P_{an}	Analysis constraint
P_{en}	Energy constraint
P_g	Geometric constraint
P_{manuf}	Manufacturing constraint

q	Hourglass mode magnitude
Q	Force (or moment) conjugate to q
s	Scaling factors
t_f	Duration
u	Displacement
U	Strain energy absorbed by the bar and the spring
U_b	Energy absorbed by the beam
U_s	Energy absorbed by the spring
v	Velocity
V	Volume
w_i	Weighting constants
$w(x)$	Distributed load
γ_{eq}	Slip rate
$\Delta\bar{\epsilon}^{pl}$	Increment of the equivalent plastic strain
ϵ	Equivalent strain field
$\bar{\epsilon}$	Mean of equivalent strain field
$\bar{\epsilon}_f^{pl}$	Critical equivalent fracture strain
$\dot{\epsilon}_{ij}$	Strain rate tensor
$\bar{\epsilon}_o^{pl}$	Initial equivalent plastic strain
$\bar{\epsilon}^{pl}$	Equivalent plastic strain
$\dot{\bar{\epsilon}}^{pl}$	Equivalent plastic strain rate
μ	Friction coefficient
μ_k	Kinetic friction coefficient
μ_s	Static friction coefficient
ρ	Density
σ_{ij}	Stress tensor
$\bar{\sigma}$	Effective stress
$\bar{\sigma}_0$	Initial yield stress
Ω_i	Damage parameter

LIST OF ACRONYMS/ABBREVIATIONS

ANN	Artificial Neural Network
DoE	Design of Experiment
EuroNCAP	The European New Car Assessment Program
FE	Finite Element
IPM	Ideal Point Method
ODB	Offset Deformable Barrier
ORB	Rigid Deformable Barrier
RSM	Response Surface Methodology
SMC	Sheet Moulding Compound

1.   INTRODUCTION

Thin-walled tubes are used in many structural applications to provide protection against impact loads. In automotive industry, thin-walled tubes like bumper beams are used as shock absorbing parts. They are attached to the front and rear ends of motor vehicles by means of brackets, which act as crash-boxes by taking the loads mainly in the axial direction. These parts need to be designed to minimize the damage to the vehicle and the risk of injury to the occupants by absorbing the energy stemming from collisions. Their effectiveness under such impact loads is called crashworthiness. Better crash performance of the bumper-beam and the crash-boxes reduces the effect of crash transmitted to the other components, and thereby protects them from further damage and saves the occupants from severer injury. Existing bumper-beams and crash-boxes are generally box-shaped for increased impact resistance. However, their cross-sectional profile can be modified to further improve their impact performance. This requires, first, a realistic simulation of their behavior under crash, and then design optimization.

1.1. Thin-walled Beams under Transverse Impact Loads

A number of researchers developed simulation models for bumper-beams under impact conditions. Kokkula *et al.* [1] considered the anisotropy stemming from manufacturing processes and the effect of strain rate in the analysis of bumper beams subjected to transverse impact loads in order to obtain a realistic finite element model. They also validated the numerical model by comparing the results with the experimental data obtained by Kokkula *et al.* [2]. Liu and Day [3] modeled bumper beams under impact loads both numerically and analytically. In their numerical study, they neglected the frictional effects. They verified their simulation model by comparing the results with impact test data and results of an analytical model. Marzbanrad *et al.* [4] studied the effects of material, shape, thickness, and impact conditions on bumper-beams subjected to low-velocity impact. The materials considered in their study were aluminum, glass mat thermoplastic (GMT) and high strength sheet molding compound (SMC).

Some other researchers, on the other hand, conducted, besides modeling, design optimization studies to improve the performance of bumpers. Patel *et al.* [5] carried out topological optimization of straight and curved bumper beams subjected to static and dynamic loads using hybrid cellular automata (HCA). In the case of dynamic loading, curved beams hitting a rigid wall at 5 m/s were considered. The constitutive relation was modeled using piece-wise stress-strain curves. However, the strain rate effect was not included in the model. Farkas *et al.* [6] found an optimal geometry for dual-channel bumper beams hitting rigid barriers at 16 km/h for offset frontal impact and at 15 km/h for pole frontal impact. Cross-sectional profile is defined using straight lines with seven geometric parameters. They created a meta-model and carried out a multi-objective optimization. Their objective was to minimize the weight and at the same time achieve force uniformity. They imposed constraints on the peak force and the largest intrusion in the bumper beam. In another study, Farkas *et al.* [7] considered the same problem and improved the model by including the effects of parametric uncertainties. Duponcheele and Tilley [8] conducted a topology optimization study using genetic algorithm to maximize the area moment of inertia of a bumper beam; but not considered a crash event. Zhang *et al.* [9] used a multi-objective formulation for optimum crash performance of rib-reinforced thin-walled hollow square beams under three-point bending drop test with a speed of 36 km/h. They used the feasible direction method as well as the ideal point method. The profile of the reinforcing rib was defined by spline curves with three variables while the outer shape is not varied. Zarei and Kroger [10] optimized the bending behavior of filled and empty hollow beams with rectangular cross section under impact loads using wall thickness and base dimensions as design variables; in other words, they optimized the size not the shape of the beam. They employed response surface methodology to build a meta-model, then, using genetic algorithm, they maximized the total energy absorption and specific energy absorption. They also conducted three-point bending tests under impact loading to compare the numerical and experimental results. Shin *et al.* [11] took lower-leg form impact test and Federal Motor Vehicle Safety Standards (FMVSS) Part 581 into consideration in the design of bumper-beam. Their model included a plate connected to the bumper beam with three springs. They optimized the thicknesses of these parts and the stiffnesses of the springs in order to minimize the weight while satisfying the

constraints on upper tibia acceleration of a pedestrian hit by a car and intrusion and deflection of the bumper beam. Mullerschon *et al.* [12] carried out a topology optimization of the bumper beam based on HCA under the conditions of a mass barrier hitting the bumper beam with a velocity of 16 km/h to get uniform strain energy density, and then the resulting design was transformed into a thin wall structure which was modeled with shell elements. This part was considered as having four different subsections with different thicknesses. These four thickness parameters were optimized in order to satisfy the maximum force constraint. Kim *et al.* [13] optimized the topology of a frontal back beam reinforcement of a bumper beam to obtain uniform strain energy density in the bumper beam. They simulated full frontal and corner tests. Using response surface methodology, they created a surrogate model. Then, without changing the overall shape of the bumper beam, they varied the overall dimensions of the reinforcement to minimize the repair cost of the car after collision. They also imposed constraints on the intrusion, back beam deflection, and back beam height variation.

There are also studies [14–17] that tried to minimize the risk of injury to pedestrians; but this is achieved generally by optimizing low-stiffness parts in the front of the bumper beam not the bumper beam itself, which is too rigid to have an effect in that respect.

In some of the published studies [1–4], only crash phenomena were modeled. The ones that included optimization of the bumper beam [5–9, 11, 12] considered the problem under low collision velocities. Only Zarei and Kroger [10] considered high collision velocities (45 km/h) under a three-point bending drop test; but they just conducted a size optimization study. The loading conditions of the bumper beams considered in the previous studies were pole frontal impact [5, 9, 10] and central frontal impact [11]. Moreover, the past studies mainly concentrated on size and thickness optimization except for a few topological [5, 8] and shape [6, 9] optimization studies. There is only one study [7] that modeled 40% offset impact test, but with an impact velocity of 16 km/h.

All in all, the previous studies did not fully simulate the standard high-speed test

conditions. One may not assume that the optimum shape designs obtained for low impact velocities are also optimum for high velocities. Although, the collision energy is not absorbed solely by the bumper beam at high collision speeds, impact energy absorbing capacity of the bumper beam will have an effect on the overall crashworthiness of the whole vehicle. Satisfaction of the requirements on the crash performance of the bumper for low velocity collisions is just sufficient. The effective way of optimally designing bumper beams is to maximize their crashworthiness at high speeds, thus providing the maximum protection for the passengers, while setting a constraint on their low-speed crash performance.

1.2. Thin-Walled Tubes under Axial Impact Loads

As for the tubes under axial impact loading, there are a number of studies in the literature on the optimization of tubes made of metals (usually steel and aluminum) under axial impact loading. In these studies, tubes are considered either as empty [18–31] or filled [29,32–40]. Yamazaki and Han [18] studied square and cylindrical tubes hitting a rigid wall with a velocity of 10 m/s. They maximized the total energy absorption while maintaining the mean crushing force at a certain limit by varying the thickness of the tube and the section radius. Lee *et al.* [19] studied tubes with circular cross-section hitting a rigid wall with a velocity of 10m/s and additional mass of 500 times the mass of the tube. Their design parameters were wall thickness, radius, and the length of the tube. Sheriff *et al.* [20] used the bottom diameter, height, and taper angle as design variables to maximize the total energy absorbed in circular cross-section tubes. Avalle and Chiandussi [21] optimized cylindrical tubes with tapered tip for uniform reaction force distribution. They varied the length of the tapered tip and tip diameter. Hou *et al.* [22, 23] optimized square and hexagonal single-cell and multi-cell tubes using base dimensions and thickness as design variables for minimum peak force and maximum specific energy absorption, i.e. energy absorption per unit mass. Acar *et al.* [25] varied taper angle and number of ribs on the surface in order to maximize the ratio of the mean crush force to the peak force and specific energy absorption. Qi *et al.* [26] analyzed single and multi-cell square tubes under oblique impact. Their objective was to increase the specific energy absorption and minimize the peak crushing force by

changing the taper angle and wall thickness. Liu [27] optimized the wall thickness and side length of a box-shaped column to maximize the specific energy absorption with a constraint on the peak force. Liu [28] considered straight and curved octagonal and hexagonal tubes and selected the side length and the wall thickness as variables. The objective was to maximize specific energy absorption of the columns while constraining the peak force. Yang and Qi [29] studied empty and filled tubes with a square cross-section under axial or oblique impact. Their objective was to increase the specific energy absorption and minimize the peak crushing force by varying the wall thickness, cross-section width, material yield strength, and filler material density. Zarei and Kröger [30] optimized empty cylindrical tubes by taking their length, diameter, and thickness as design variables for increased total energy and specific energy absorption. They extended that study to tubes filled with honeycomb [33] and foam [34] by considering their densities as variables. Kim and Arora [31] studied representation of tapered tubes with uniform ones with square-sections in the force-displacement domain. With these force representations, a model with a single degree of freedom that simplified the analysis of the tube structure was identified. Santosa and Wierzbicki [32] studied the axial crushing resistance of a square-box column filled with aluminum honeycomb or foam under quasi-static loading conditions. Sun *et al.* [37] optimized crash-boxes with functionally graded foams for maximum specific energy absorption and minimum peak force. They assumed the foam material as layered and they varied the density of these layers. Hanssen *et al.* [35] used formulas derived based on experimental data relating design parameters to average force, maximum force, and stroke efficiency in order to obtain optimum designs of columns for minimum reaction force and maximum energy absorption. Ahmad and Thambiratnam [36] conducted a parametric study on empty and foam-filled tubes under axial impact loads using the wall thickness, taper angle, foam density, impact mass, and impact velocity as variables. Yin *et al.* [38] studied honeycomb-filled single and bi-tubular polygonal tubes. The variables were the wall thickness and side length. The objective was to maximize the specific energy absorption and to minimize the peak force. Bi *et al.* [39] studied foam-filled single and multi-cell hexagonal tubes, which were crushed under a rigid wall moving downward with a velocity of 2 m/s and penetration depth of 100 mm. The variables were chosen to be the wall thickness and the side length of the section, and the foam density. The

objective was to increase the specific energy absorption while keeping the mean crushing force larger than a certain limit to ensure a certain structural rigidity. Tarlochan *et al.* [40] conducted a parametric study on foam filled tubes under axial and oblique impact loading. They compared tubes having circular, square, hexagonal, octagonal, ellipsoidal cross-sections with the same circumference in terms of energy absorption and crush force efficiency.

The previous researchers generally developed approximate expressions for the objective functions using response surface methodology [18–23, 25–28, 30, 33, 34, 37–39], Kriging [29], moving least-squares approximation [31], and artificial neural network [24]. After obtaining the surrogate models, they used genetic algorithms [20, 33, 34], leapfrog [24], particle swarm optimization [26,29,37,38], non-linear programming [22,23,25], or multi-first order method [21] as search algorithms.

The cross-sectional shapes of the tubes considered by the researchers were circular [18–21, 25, 30], square [18, 22, 24, 26, 27, 29, 33–37], hexagonal [23, 28, 38–40], or octagonal [28, 38]. Some of the previous studies focused on straight columns with uniform cross-section along the length [18, 19, 22–24, 26–30, 33–35, 37–39]; some of them introduced taper angles [20, 21, 25, 36], and some [24, 25, 33, 34] introduced ribs with predefined shapes.

In the present study, a larger number of geometric parameters are used as optimization variables in comparison to the previous studies. The parameters defining the shape of the cross-sectional profile (the coordinates of key points defining the spline curves) and the longitudinal profile (depths and widths of the circumferential ribs, and the taper angle), and the wall thickness are varied. To the authors' knowledge, the shapes of the ribs are optimized for the first time in this study; in the previous studies, on the other hand, they were taken as constant. The ribs can be inward or outward. The taper angle can be positive or negative. Besides, the loading conditions considered in almost all the previous studies were either drop tests i.e. an object being dropped on a column, or a column with a mass at the rear hitting a rigid wall. In this study, the methodology developed for the optimum shape design of tubular structures

is applied to the crash-boxes (or brackets) holding the bumper beam of a vehicle. The behavior of the crash-box is simulated for the loading conditions in a standard high-speed crash test, European New Car Assessment Program, (EuroNCAP). Because of the difficulty in modeling the whole car and the resulting long computational times, a lumped-parameter car model is developed that accounts for the structural behavior of the main body of the vehicle as well as the parts in front of the crash-box. Moreover, in this study, a hybrid of genetic algorithm (GA) and Nelder-Mead algorithm is developed to find the globally optimal design or a near global optimal design.

The goal of global design optimization is to find the design with the best possible performance. This requires a definition of the geometric design that allows significant changes in shape, i.e. the solution domain should be large so that it includes the designs leading to the highest possible levels of performance. This means the number of geometric parameters and the range of values that can be assigned to these parameters by the search algorithm should be large. Global shape optimization of a vehicle for maximum crashworthiness is infeasible considering the high number of interacting parts, the high number of parameters used to define their geometries, and complex interactions among them during crash. This is beyond the capabilities of the current state-of the-art computers and search algorithms. Considering the computational effort to simulate crushing of the whole vehicle, it is not possible to find the globally optimum design within such a large solution domain and with such a large number of design variables even if a powerful global search algorithm is used. If large changes are allowed in the values of the optimization variables during optimization, the accuracy of surrogate models will also be questionable even for a single part let alone the whole vehicle. Besides, if the individual parts are separately optimized, loading conditions on them will be different from that of a drop test. That means the shape of a part optimized for the loading conditions in a drop test will not be optimum for the loading conditions in a real crash test.

The procedure suggested in this study to surmount these problems is as follows: Individual parts of the vehicle are optimized via a reliable global search algorithm by using a high number of design variables and allowing large changes in the values

of these variables. The remaining parts of the vehicle are modeled with a system of lumped masses, springs, and dampers using parametric system identification; therefore computational times will not be prohibitively long. At the last stage, the whole vehicle is optimized starting from the optimized shapes of the individual parts; but this time, the ranges of values that can be assigned to the variables will be small; some of the parameters may be taken as constant. Then, it becomes feasible to develop a reliable surrogate model for the vehicle and perform optimization. In this study, modeling and design optimization of two parts, crash-box and bumper-beam, are considered.

2. PROBLEM STATEMENTS

Bumper-beams and crash-boxes are designed to perform under collision. Naturally, the number of different obstacle types the tubes suffer during frontal impact is endless. However they can be classified as

- Full frontal collision
- Offset frontal collision
- Pole frontal collision

For the bumper-beam, the harshest one among the three scenarios is the pole, however it is also the rarest among them. The second harshest one is offset impact. And the majority of the frontal collisions happen with an offset with varying percentages [41]. Considering the severity and frequency of the three major frontal crash scenarios, bumper-beam is optimized for an offset frontal collision in accordance with EuroNCAP, IIHS, ANCAP standard tests (See Figure 2.1).

The bumper-beam is supported by two crash-boxes at two sides; they are in turn fixed to the main frame of the car. The harshest collision a bracket endures is the offset frontal impact, where one of the brackets takes the impact energy. Accordingly, the crash-box is optimized for offset collision conditions in accordance with EuroNCAP, IIHS, ANCAP standard tests, where the vehicle hits a wall with 40% offset and 64 km/h speed (See Figure 2.1).

Figure 2.1. A scheme for EuroNCAP Frontal offset crash tests [42].

The objective of this study is to develop a methodology to find the globally optimum shape or near globally optimum shapes for the cross-sectional profile of the

bumper-beam and the cross-sectional and the longitudinal profiles of the crash-box to maximize their crash performance under the loading conditions in EuroNCAP tests.

3. APPROACH

The effectiveness of design optimization depends on the proper choice of the objective function. Improving its value should enhance the structural performance of the part in the most effective way.

3.1. Objective Functions

3.1.1. Objective Function for the Bumper-Beam Optimization

A metric is defined that is a measure of the crashworthiness of the bumper beam. Depending on the choice of the metric, different outcomes are obtained for the optimum part design. As a measure of crash performance, the objective function to be increased is defined in this study as

$$f_{obj} = \frac{w_1}{n_1} \int_0^{t_f} \iiint_V \sigma_{ij}\dot{\epsilon}_{ij}dVdt - \frac{w_2}{n_2}\sqrt{\frac{1}{V}\iiint_V (\epsilon - \bar{\epsilon})^2 dV} - P \qquad (3.1)$$

where V is the volume of the bumper beam, σ_{ij} is the stress tensor, $\dot{\epsilon}_{ij}$ is the strain rate tensor, ϵ is the equivalent strain field, $\bar{\epsilon}$ is ϵ's mean value, t_f is the duration for which the simulation is conducted starting from initial contact with the barrier, w_i are the weighting constants. The values of w_i are chosen in accordance with the relative importance that the designer gives to the individual terms; n_i are the normalization constants having values 3215 J and 600, respectively, which are the strain energy absorbed by the bumper beam currently in use and the variation in equivalent strain. The first term is the total internal energy of deformation in the bumper beam during crash. The larger the first term, the larger is the portion of the collision energy taken by the bumper. The second term is a measure of uniformity in the deformation. This term is introduced to bias the configurations in which deformation is more uniform. The smaller is this term, the more uniform is the deformation; accordingly, the integrity of the bumper - bracket system is expected to be better maintained. P is the penalty

function, which includes the following terms

$$P = P_{an} + P_g + P_{manuf} + P_{mass} \tag{3.2}$$

P_{an} is the analysis constraint, which is activated when finite element analysis fails due to sharp corners or some other reason. P_g is the geometric constraint, which is activated when a cross-sectional profile selected by the search algorithm does not fit the allowable spacing. P_{manuf} is the manufacturing constraint. If the profile of the cross-section contains sharp curvatures that pose difficulties in manufacturing, P_{manuf} becomes active. If P_g and P_{manuf} become active, a large value is added to the objective function without calculating the other terms. P_{mass} is the mass constraint such that

$$P_{mass} = \begin{cases} 0 & \text{if } m \leq m_{ben} \\ 1000(\frac{m-m_{ben}}{m_{ben}})^2 + 100(\frac{m-m_{ben}}{m_{ben}}) & \text{if } m > m_{ben} \end{cases}$$

m is the mass of the bumper, m_{ben} is the mass of the bumper beam in current use, which is taken as a benchmark value. The constants are chosen such that the term gives small penalty values for small violations but the penalty value increases quadratically for large violations. Mass constraint is introduced in order to avoid optimal designs that show increased crashworthiness over the beam currently in use at the expense of increased weight. By adding the penalty terms into the objective function, the constrained problem is transformed into an unconstrained one.

The objective of the metric above is to find the best shape of the cross-sectional profile which allows the bumper to absorb significant impact energy and also avoids development of extreme plastic strains leading to rupture in the bumper while ensuring that this is achieved without increasing the mass of the bumper beam.

3.1.2. The Objective Function for the Crash-Box Optimization

The following objective function is chosen in the crash-box optimization:

$$f_{obj} = \frac{w_1}{n_1} \frac{1}{\rho V} \int_0^{t_f} \iiint_V \sigma_{ij} \dot{\varepsilon}_{ij} dV \, dt - \frac{w_2}{n_2} \sqrt{\frac{1}{V} \iiint_V (\varepsilon - \bar{\varepsilon})^2 dV}$$
$$- w_3 \left(\frac{1}{2n_{31}} F_{max} + \frac{1}{2n_{32}} \frac{\Delta F_{max}}{\Delta t} \right) - P \tag{3.3}$$

where V is the volume of the crash-box, σ_{ij} is the stress tensor, $\dot{\epsilon}_{ij}$ is the strain rate tensor, t_f is the duration for which the simulation is conducted starting from the initial contact with the barrier, ε is the equivalent strain, $\bar{\varepsilon}$ is its mean value, F_{max} is the maximum force at the rear of the crash-box that occurs in the first 0.5 ms of the collision, Δt is the time that passes until the maximum force occurs. The first term is the specific internal energy, or the energy absorbed per unit mass of the crash-box during crash. It is a measure of how effectively it takes the collision energy. The second term is a measure of uniformity in the deformation. This term is introduced to avoid shapes that result in highly localized deformation. The smaller is this term, the more uniform is the deformation; accordingly, the integrity of the tube is expected to be better maintained. The third term includes the magnitude of the peak force during the first 0.5 ms, F_{max}, as well as the average rate of increase in force, $\Delta F_{max}/\Delta t$. During collisions, generally the force transmitted reaches a peak value at the initial stages of the impact. It is essential to reduce the magnitude of the peak force as well as the rate of increase in force during the initial phases of the collision to reduce the jerking effect felt by the occupants during impact. w_i are the weighting constants; their values are chosen according to the relative importance that the designer gives to the individual terms; n_i are the normalization constants, which are $n_1 = 38.1$ J/g , $n_2 = 1195$, $n_{31} = 156.7$ kN, and $n_{32} = 991.8$ MN/s. These values are obtained from the simulations conducted for a 70 mm-diameter circular tube, which is taken as benchmark. P is the penalty function, which includes the following terms:

$$P = P_g + P_{mass} + P_{en} + P_{an} \tag{3.4}$$

P_g is the geometric constraint, which is activated when a cross-sectional profile generated by the search algorithm does not fit the allowable spacing. If P_g becomes active, a large value is added to the objective function without calculating the other terms. P_{mass} is the mass constraint such that

$$P_{mass} = \begin{cases} 0 & \text{if } m \leq m_{ben} \\ 1000(\frac{m-m_{ben}}{m_{ben}})^2 + 100(\frac{m-m_{ben}}{m_{ben}}) & \text{if } m > m_{ben} \end{cases}$$

m is the mass of the crash-box, m_{ben} is the mass of the benchmark structure. The mass constraint is introduced in order to avoid optimal designs that show increased crashworthiness over the benchmark design at the expense of increased weight. P_{en} is the penalty introduced to eliminate the designs taking a lower impact energy in comparison to the benchmark case. Its value is calculated as

$$P_{en} = \begin{cases} 0 & \text{if } \bar{E}_{acc} \geq \bar{E}_{ben} \\ 3600(\frac{\bar{E}_{ben}-\bar{E}_{acc}}{\bar{E}_{ben}})^2 + 450(\frac{\bar{E}_{ben}-\bar{E}_{acc}}{\bar{E}_{ben}}) & \text{if } \bar{E}_{acc} < \bar{E}_{ben} \end{cases}$$

$\bar{E}_{acc}$ is the total accumulated energy in the crash-box, $\bar{E}_{ben}$ is the benchmark value for energy. P_{mass} and P_{en} are formulated such that the terms yield small penalty values for small violations; but the penalty value increases quadratically for large violations. P_{an} is the analysis constraint, which is activated when finite element analysis fails due to sharp corners or some other reason. By introducing the penalty terms, the constrained optimization problem is transformed into an unconstrained one.

The above metric is formulated to find the best shape that maximizes the specific energy absorption, avoids development of extreme plastic strains leading to rupture in the structure and also reduces the peak force and its jerk effect while ensuring that this is achieved by keeping the total energy absorption above certain limit without increasing the mass.

3.2. Defining the Shape and Optimization Variables

3.2.1. Bumper-Beam

In this study, considering that bumper beam is manufactured through an extrusion process and thus cross-sectional profile is not varied along its length, only the shape of the cross-sectional profile of the bumper beam is optimized. Spline curves are used to define the profile. Accordingly, the optimization variables are the coordinates of the key points used to define the spline curves. In Figure 3.1, a typical cross-section is shown. Only the frontal regions of the bumper are optimized, because it is fastened to the brackets having a given geometry by means of bolts from its back. As seen in the figure, the profile is defined by six key points. Five of them are free to move only in the x-direction; one of them can move in both directions. By changing the positions of the key-points, the shape of the profile is changed. During the optimization, the optimal positions of the key-points are found so that the bumper will have the highest crashworthiness according to Equation 3.1.
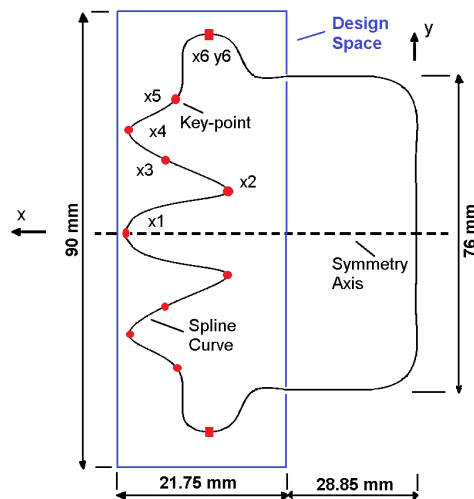
Figure 3.1. Defining the cross-sectional profile of the bumper beam by spline curves described by six key points with seven variables.

Due to size limitations, the key points are allowed to move within a given domain. If the algorithm assigns a position for a key point outside this domain, a penalty value is added to the objective function. The spacing enclosing the current design of the bumper beam (Figure 3.1) is adopted as the region within which the key points freely

move.

3.2.2. Crash-Box

In the present study, the shapes of both the cross-sectional profile and longitudinal profile are varied as well as the wall thickness of the crash-box. Making use of the double symmetry of the cross section with respect to the x and y axes (Figure 3.2a), only the shape of one quarter is defined by a spline curve using three key points. Point 1 is allowed to move only horizontally; point 3 only vertically; on the other hand, point 2 can move in both directions. The longitudinal profile is defined by a series of coefficients as well as three length parameters. The first coefficient is the taper coefficient, c_α, which is used to define the taper angle, α. c_α is the ratio of the radial coordinates of the base and end-section key points. Furthermore, up to three ribs can be created at predefined locations along the crash-box. The profiles of the ribs are constructed using cubic spline curves, which are described by key points defined by depth coefficients, r_i, and length parameters, l_i, (See Figure 3.2b). $r_i \times c_\alpha$ is the ratio of the radial distance of the key point at the ith rib to that at the base. With the help of $r_i \times c_\alpha$, the depths of the ribs, h_i are defined. The taper coefficient, c_α, can take values larger or smaller than 1.0. Accordingly, taper angle, α, can be positive or negative. Similarly, h_i may take positive or negative values; the ribs may then be inward or outward. Due to size limitations, constraints are imposed on the design variables such that the key points may not go outside the domain shown in Figure 3.2a. In addition to the outer boundary of the design space, the key points defining the base cross-sectional profile are not allowed to enter the inner circular region with 12 mm radius in order to avoid numerical difficulties. The dimensions of the outer boundary are chosen based on the dimensions of a crash-box currently used in a Renault car. If the algorithm assigns a position for a key point outside this domain, a large penalty value, P_g, is assigned to the objective function.
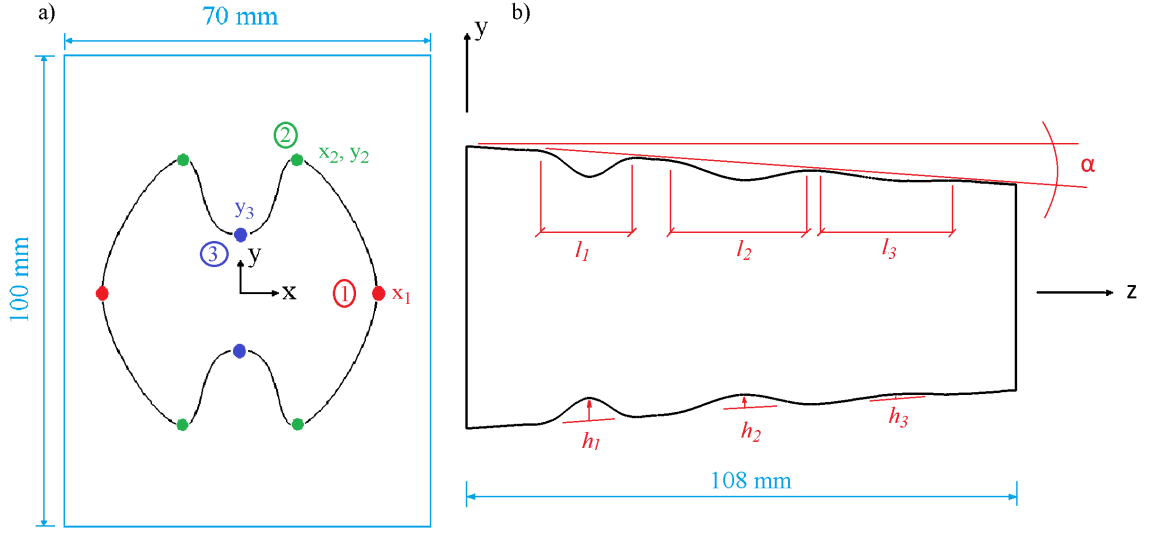
Figure 3.2. Defining the cross-sectional (a) and longitudinal (b) profile of the tube by spline curves.

3.3. Modeling of the Barrier

EuroNCAP uses a deformable barrier made of aluminum honeycomb in frontal offset-impact tests. The deformable barrier is designed to simulate an average collision partner during an accident. Although quite complex structural problems can be solved by FEM, analysis time should not be long in design optimization studies where thousands of runs may be needed to locate the globally optimum design or a near globally optimum design. For this reason, the barrier is modeled as rigid in the simulations. Because a rigid barrier does not absorb any impact energy, the effect of collision is severer. Deb *et al.* [43] used a lower velocity for the car in their simulations in order to account for the effect of deformable barrier. However, in this study, a lower mass is used for the car such that the severity of impact is more or less the same. The energy balance equation for collision of a vehicle with a deformable barrier can be written as

$$\frac{1}{2}mv_0^2 = E_{vint} + E_{vke} + E_{bar} \tag{3.5}$$

where v_0 is the initial velocity of the vehicle, m is its original mass, E_{vint} is the energy absorbed by the vehicle, E_{vke} is the final kinetic energy of the vehicle after impact, and E_{bar} is the energy absorbed by the deformable barrier.

If the vehicle hits a rigid barrier with the same velocity, v_0, but with a different mass such that the same amount of energy, E_{vint}, is absorbed by the vehicle, then the equation becomes

$$\frac{1}{2}m'v_0{}^2 = E_{vint} + E'_{vke} \tag{3.6}$$

Here, m' is the equivalent vehicle mass and E'_{vke} is the final kinetic energy of the vehicle after impact. It now follows from Equations 3.5 and 3.6 that

$$m' = m - \frac{2}{v_0^2}(E_{bar} + E_{vke} - E'_{vke}) \tag{3.7}$$

Assuming $E_{vke} \approx E'_{vke}$, the above relation becomes

$$m' \approx m - \frac{2}{v_0^2}(E_{bar}) \tag{3.8}$$

According to Deb *et al.* [43], the ratio of the energy absorbed by the deformable barrier in a conventional offset test to the vehicle mass, E_{bar}/m, does not change much for cars of various mass. Taking E_{bar}/m as 82 J/kg as suggested by Deb *et al.* [43], m' is found to be $0.483m$; but to be on the safe side, it is taken as $0.5m$. The mass of the vehicle is 1116 kg (904 kg $+2 \times 88$ kg $+36$ kg, which are the masses of Hybrid-III dummies of 88 kg and a luggage of 36 kg). So the effective mass, m', is 558 kg. In the simulations, the car hits a rigid wall with an initial velocity of 64 km/h (17.8 m/s) and 40% offset.

Here, it is noteworthy that to develop a simplified model for the barrier is, needless to say, an option. However, the computational burden of that model would not be as much as it is needed in this study. Further, using a rigid model of the barrier makes the localization effect severer which, in turn, forces better designs for the bumper-beam under localized loadings like pole frontal impact etc. That is one of the reasons that, as will be shown later, good results for the tests.

3.4. Modeling of the Main Vehicle Body

Another concern is the modeling of the main vehicle body for the optimization of the bumper-beam and the crash-box cases.

3.4.1. Bumper-Beam Case

One option is to model the whole car as a deformable body in full detail; but this takes excessively long computational times. Considering that optimization process may require quite a number of iterations, modeling the whole car is not a feasible option.

Another alternative is to include only the bumper-bracket system in the finite element model as deformable parts and account for the inertia effects of the rest of the vehicle by two rigid mass blocks fastened to the ends of each crash-box (See Figure 3.3). Although this approach is computationally effective, the accuracy of its results is questionable because no energy is absorbed by the rest of the vehicle.
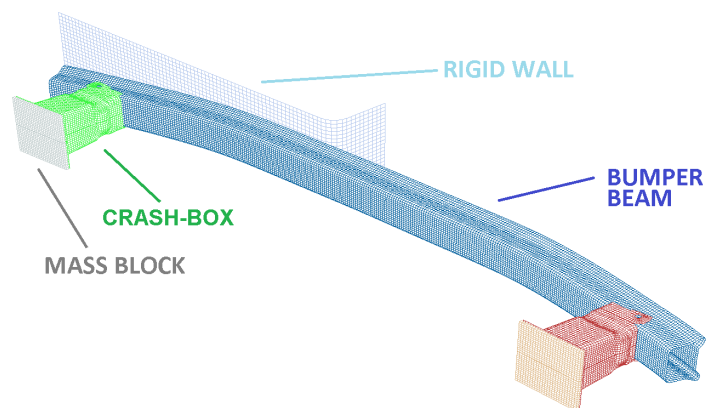
Figure 3.3. The assembly of the system with mass blocks.

In this study, knowing that these two approaches are not applicable, a lumped parameter model is developed consisting of lumped masses, springs and dampers to account for the deformation and the energy absorption behavior of the rest of the car behind the brackets.

A number of simplified models were developed by researchers to simulate the crash behavior of vehicles using dynamic system identification. The models can be classified

as linear [44–47] or nonlinear [48,49], which may be parametric [45,46] or nonparametric [44,47–49]. The loadings considered in those studies were either symmetric [44–48] or asymmetric [44,49]. Crash phenomena were considered either at low-speed [45,46,48] or high-speed [44,46,47,49]. Models were tuned based on the objectives of acceleration [44,46,47], intrusion/displacement [44,45,49], force [48], energy absorption [49], and weight [44,49]. The models were either single [46,47] or multi-objective [44,45,48,49].
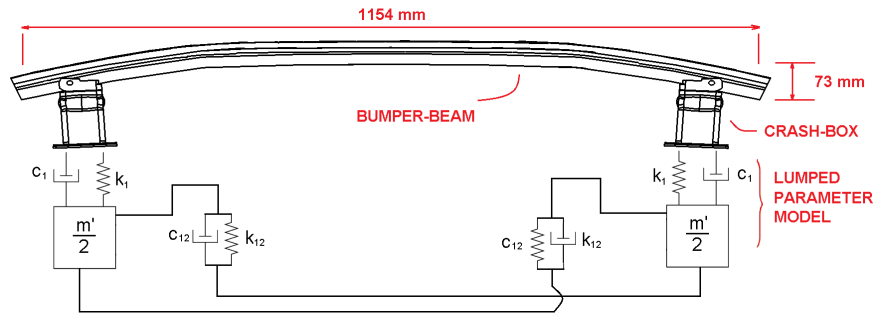
Figure 3.4. A depiction of the lumped parameter model for the car structure.

Figure 3.4 shows a depiction of the model used in this study. The model parameters are k_1, c_1, k_{12}, c_{12}, where k_1 and c_1 denote the spring and damping effects behind the crash-boxes; while k_{12} and c_{12} denote the spring and damping effects between the different sides of the car during their relative movement. Because at the early stages of the impact plastic deformation mainly occurs in the bumper beam, then in the crash-box, after that in the remaining structural parts of the vehicle, the main body is assumed to be linearly elastic and its mechanical response can be represented by linear springs during early phases of the collision during which the simulations are continued.

In order for the lumped parameter model to represent the behavior of the car during collision, suitable values for the model parameters must be chosen. For this purpose, the results of the present lumped parameter model of the car structure are made to match that of the full finite element model of 2010 Toyota Yaris (Sedan), which was developed and validated by The National Crash Analysis Center (NCAC) of the U.S. [50]. This car model is crashed into a rigid wall with an offset according to the scenario specified above but with a reduced speed (12.5 m/s) to account for the effect of rigid wall.

The lumped parameter model is assembled with the bumper beam and the crashboxes as depicted in Figure 3.4. The mass blocks are positioned so that the mass center of the lumped parameter model coincides with that of Yaris model. Because rotation of the vehicle occurs in the last stages of impact, rotational inertia of the vehicle is assumed not to affect the deformational behavior of the vehicle during the initial stages of impact for which simulations are conducted. Finite element simulations are conducted according to the collision scenario described above. The resulting reaction forces on the rigid wall due to the collision are calculated as a function of time. The model parameters are optimized so that the impact forces on the wall obtained using the full car model and the lumped parameter car model are as close to each other as possible. In order to judge the closeness of the two outcomes the following measure is used, which is the sum of the differences in the impact forces at corresponding time intervals.

$$f_{obj} = \sqrt{\sum_{i=0}^{100} \left[F\left(t_0 + \frac{t_f - t_0}{100}i\right) - \tilde{F}\left(t_0 + \frac{t_f - t_0}{100}i\right) \right]^2} \tag{3.9}$$

where t_0 is the initial time, t_f is the final time. F is the resulting impact force for Toyota Yaris model on the wall, $\tilde{F}$ is the impact force for the lumped parameter model.
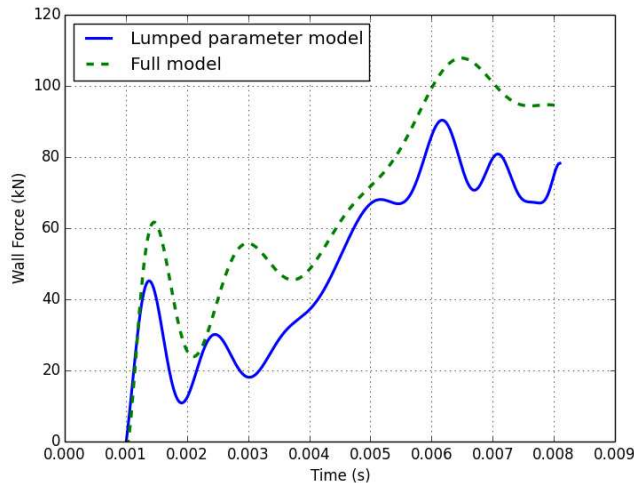
Figure 3.5. Comparison of the reaction forces at the barrier resulting from car crash for the simplified lumped parameter model developed in the present study and the full finite element model provided by the National Crash Analysis Center (NCAC) [50].

The values of k_1, c_1, k_{12}, c_{12} are optimized to yield minimum f_{obj}. This opti-

mization problem is solved using Nelder-Mead as search algorithm. As depicted in Figure 3.5, the results of the lumped parameter model approximate that of the full car model. The differences may be attributed to the differences in the bumper model. The optimum values of the parameters, k_1, c_1, k_{12}, c_{12}, are found as $854.4 \ 10^6$ N/m, $193 \ 10^3$ N s/m, $609.7 \ 10^6$ N/m, $246 \ 10^6$ N s/m, respectively.

3.4.2. Crash-Box Case

Lumped-parameter vehicle model used in the crash-box optimization is different. Only a single crash-box is modeled as a deformable body. A lumped-parameter model is developed consisting of lumped masses, springs and dampers to account for the effects of the vehicle components behind the crash-box as well as the bumper beam in front of the crash-box, which is represented by a non-linear spring. Figure 3.6 shows a depiction of the model used in this study. Because, at the early stages of the impact, plastic deformation mainly occurs in the bumper beam and the crash-box, then in the remaining structural parts of the vehicle, the main body is assumed to be linearly elastic and its mechanical response can be represented by linear springs during early phases of the collision during which the simulations are continued.
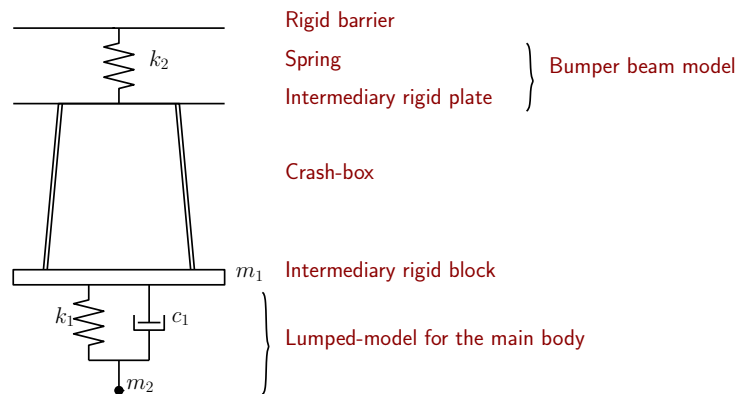
Figure 3.6. A depiction of the vehicle model.

The model parameters are k_1, c_1, k_2, m_1, m_2, where k_1 and c_1 account for the elastic deformation and damping effects behind the crash-boxes; while the effect of the deforming bumper-beam is accounted for by a nonlinear spring. The force-displacement curve of this spring is defined by a quadratic polynomial, $F(u) = au^2 + bu$, up to $u = u^*$; after that the relation becomes linear, $F(u) = cu + d$. m_1 is the mass of the intermediary

rigid plate. m_2 is the mass of the point mass such that $m_1 + m_2 = m'$. Here, the other crash-box is assumed to take no impact energy in offset impact tests.

In order for the lumped-parameter model to represent the behavior of the car during collision, suitable values for the model parameters should be chosen. For this purpose, the values of the model parameters are optimized so that the results of the present lumped-parameter car model match that of the full finite element model for 2010 Toyota Yaris (Sedan), which was developed and validated by The National Crash Analysis Center (NCAC) of the U.S. [50]. This car model is crashed into a rigid wall with an offset according to the scenario specified above.

The lumped-parameter model is assembled with the crash-box as depicted in Figure 3.4. Finite element simulations are conducted according to the collision scenario described above. The resulting reaction forces on the rigid barrier due to the collision are calculated as a function of time. The model parameters are optimized so that the impact forces on the wall obtained using the full car model and the lumped-parameter car model are as close to each other as possible. In order to estimate the closeness of the two outcomes, Equation 3.9 is used, which is the sum of the differences in the impact forces at corresponding time intervals: As depicted in Figure 3.7, the lumped-
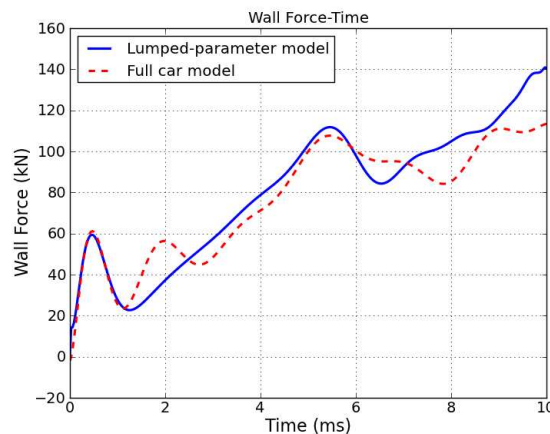
Figure 3.7. Impact forces on the barrier resulting from car crash calculated using the lumped-parameter and the full car models.

parameter model gives a response close to that of the full car model. The optimum values of parameters k_1, c_1, m_1 are found to be $1690 \ 10^6$ N/m, $145.7 \ 10^3$ N s/m, 112.79

kg, respectively. The parameters used to define the stiffness of the nonlinear spring are found to be $a = -2.9$ MN/m^2, $b = 143.7$ MN/m, $c = 1.4$ MN/m, $d = 1.6$ MN and the transition displacement is obtained as $u^* = 0.32$ mm.

3.4.3. Search Algorithm

A search algorithm is utilized to find the optimum values of the variables that yield the maximum value for the objective functions expressed in Equations 3.1 and 3.3. Considering that typical structural optimization problems contain numerous local optimums, a local search algorithm may easily get stuck at a worse local optimum rather than the global optimum. If the problem has a complex solution domain, multiple restarts may even not work. Heuristic global search algorithms, on the other hand, may find the best configuration; but they require a large number of function calls for convergence. For this reason, they are not feasible for problems requiring long computational times like crash simulations. Surrogate models may be developed using response surface method or artificial neural networks: but these models do not fully represent the response of the finite element analysis. Further, the number of design variables in this study are high requiring many finite element analysis to build the surrogate model up, which does not make the necessary simplification. In the present study, in order to search for the globally optimum design without excessive computational burden, a hybrid algorithm combining global and local search algorithms is developed. In this method, the genetic algorithm, (GA), is used to find configurations potentially close to the global optimum or one of the near global optimums. Then, these configurations are supplied to the local optimizer, Sequential Simplex (Nelder&Mead) algorithm, which in turn locates the optimum.

3.4.4. Optimization Procedure

In each iteration, new configurations are generated by the search algorithm. In order to evaluate the value of the objective function for these configurations structural analyses of the corresponding crash events are carried out. For this purpose, a FE model is developed. The FE model and the optimization algorithm are integrated

using a built-in ABAQUS python script. This code carries out FE analyses of the configurations generated by the search algorithm, writes the results on output files, and also evaluates the results to modify the values of the optimization variables according to the decision criteria of the hybrid search algorithm to obtain new candidate configurations.

Initially, the optimization code selects random values for the optimization variables within the feasible domain and creates the corresponding geometries of the crash-box as well as the bumper-beam. In this way, initial population of GA is obtained. Using the predefined velocities, boundary conditions, and the material properties, FE analyses are conducted for the randomly selected geometries. Based on the FE analysis results , the values of the objective function are calculated. The code then compares these values and selects new values for the optimization variables for the next generation according to the decision criteria of the GA. This procedure is repeated until the stopping criterion is satisfied, which requires no change in the best value found in three consecutive generations after the first 19 iterations. The initial population is taken as 300. The population is dynamic with an elitist approach; that means it is initially high; but towards the end it gets lower; however the fittest member is always maintained. Crossover and mutation probabilities are also dynamic like the population. The best points found by GA are used as initial points by Nelder&Mead algorithm, which then tries to find the best local optimum in their neighborhood. Iterations are continued until the difference between the objective function values of the best and worst configurations becomes small. This procedure is repeated starting from different random configurations to ensure that the globally optimum design or a near global optimum design is obtained.

4.   FINITE ELEMENT MODELING

Explicit FE methods are better in solving structural problems involving complex contact interactions occurring within a short duration compared to the implicit ones. Accordingly, commercial finite element program ABAQUS/Explicit is used in the present study to simulate the behavior of the parts during crash tests.

4.1. Bumper-Beam

4.1.1. Initial and Boundary Conditions

The initial and boundary conditions defined in the FE model must reflect the conditions of the crash tests. Only in this way, the response of the bumper beam can be correctly predicted. In the present FE model, the bumper beam, crash-boxes and the masses have an initial velocity of 64 km/h (17.8 m/s) as in the standard tests. The barrier on which the car hits is fixed; therefore its velocity is set to zero throughout the simulation.

The rear ends of the crash-boxes and the masses are constrained to move only in the direction of the initial velocity so as to prevent relative movement of the blocks in the transverse directions considering that the transverse displacements are almost zero during the initial phases of the crash as shown in Figure 4.1. Rotation of the vehicle occurs only at later stages of the crash.

Because the geometry and the loading are symmetric with respect to the horizontal middle plane, only the lower portion is analyzed during the optimization process and symmetry conditions are imposed on the interface.
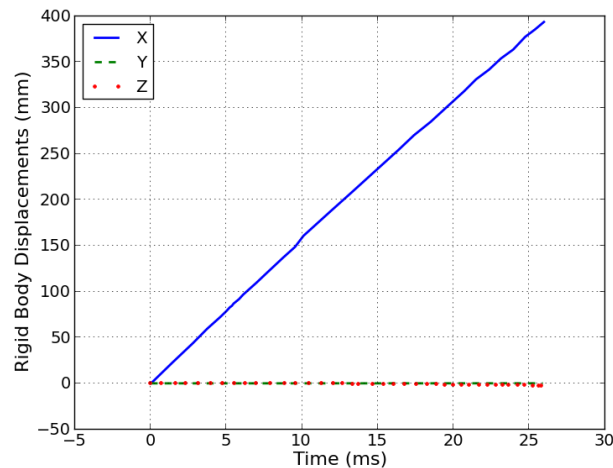
Figure 4.1. Rigid body displacement history of Toyota Yaris model [50] during initial stages of offset frontal impact.

4.1.2. Analysis Time

Because the crash occurs at a high velocity, the bumper beam and the crash boxes (brackets) cannot take the whole collision energy. Figure 4.2 shows the strain energies of the bumper beam and the left bracket as a function of time. At the initial stages of the crash, the bumper beam takes a significant portion of the impact energy, because it has a lower stiffness than the crash-box. After about 5-6 ms, the bumper collapses like a compression spring that closes solid due to an overload; thus its resistance to further deformation significantly increases. Then, the crash box begins to take the impact energy at an increasing rate. Until about 12 ms, these parts completely collapse, their stiffness greatly increases; the other parts of the vehicle connected to the bracket, then, begin to take much of the collision energy. Considering that significant portion of the strain energy absorbed by the bumper beam before the total collapse is taken in 8 ms, the simulations are continued for 8.0 ms and the energy absorbing capacity of the bumper is maximized for this duration.

4.1.3. Contact Modeling

Due to severe deformation, some parts of the bumper beam and the brackets that are not initially in contact may come into contact. For this reason, the general contact algorithm, which also accounts for self-contact, is used in order to model the contact
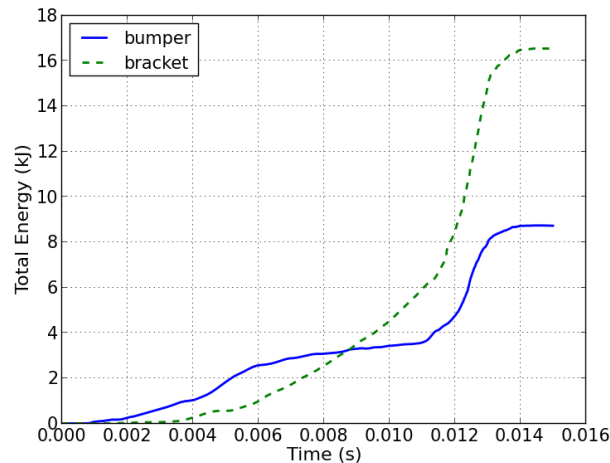
Figure 4.2. Strain energies accumulated in the bumper beam currently in use and the left bracket during the collision.

interactions in the finite element model.

4.1.4. Modeling of Fasteners

The bumper-beam and crash-boxes are fastened by means of bolts. Modeling the bolts in full detail poses difficulty because it has very complex geometry and it needs too many contact definitions. Therefore, a computationally effective bolt model needs to be used. For this purpose, the corresponding surfaces of the bumper-beam and bracket are connected with tie constraints without holes as explained in Tanlak *et al.* [51].

4.2. Crash-Box

4.2.1. Model Geometry

The finite element model includes a deformable model of one crash-box as shown in Figure 4.3. The main vehicle body is represented by a point mass, spring, damper, and an intermediary rigid block, which also serves uniform transmission of forces between the crash-box and the rest of the car. The bumper beam is represented by a nonlinear spring, which is placed between the rigid plate and the rigid barrier for uniform force transmission.
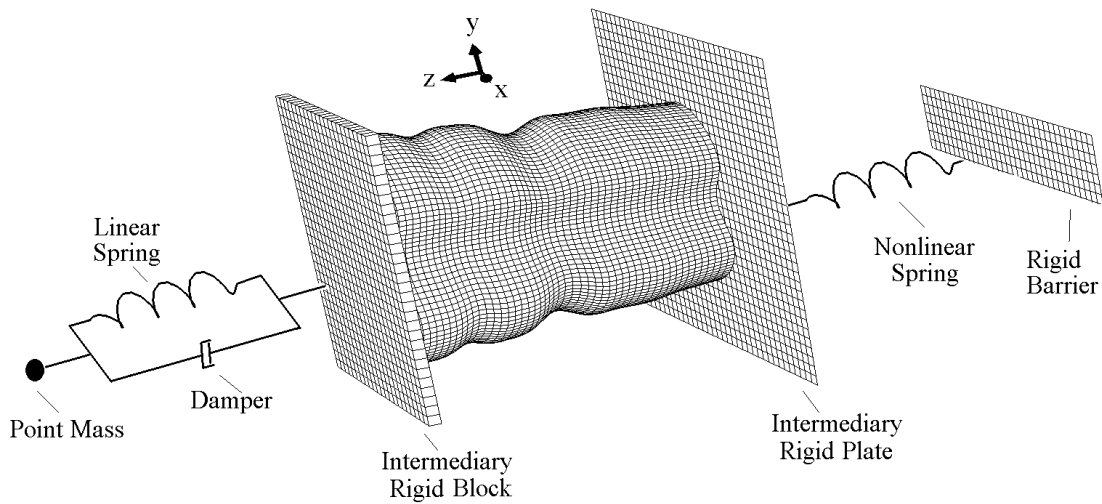
Figure 4.3. Finite element model.

4.2.2. Initial and Boundary Conditions

In the present finite element model, all parts except the rigid barrier have an initial velocity of 64 km/h (17.8 m/s). The rigid barrier which the car hits is fixed. The rear end of the crash-box and the intermediary rigid plate and block as well as the point mass are constrained to move only in the direction of the initial velocity so as to prevent relative movement of the blocks in the transverse directions considering that the transverse displacements are almost zero during the initial phases of the crash as shown in Figure 4.1. Rotation of the vehicle occurs only at later stages of the crash. Because the geometry of the crash-box and the loading are symmetric with respect to the horizontal as well as vertical mid-planes, only one quarter of the assembly is analyzed and the necessary symmetry conditions are applied on the corresponding interfaces.

4.2.3. Analysis Time

Figure 4.4 gives the energy absorbed by a circular crash-box, while Figure 4.5 shows the change in the geometry of the crash-box at 1 ms intervals. As seen in the figures, the crash-box totally collapses after 8 ms; after that its stiffness greatly increases like a compression spring closed solid due to an overload; then a much larger energy is required to induce a small deformation. At this stage, the remaining portions
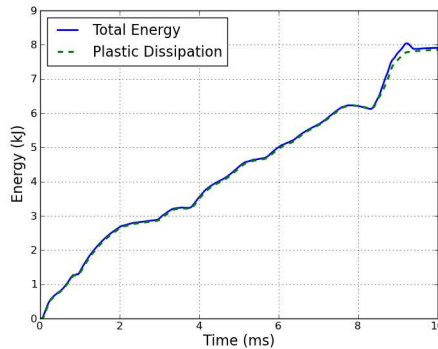
Figure 4.4. Total energy values accumulated within a typical the crash-box during the collision.
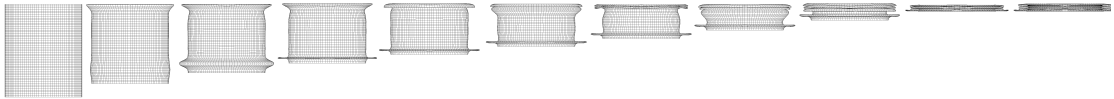
Figure 4.5. Deformation of the crash-box with a circular base shape.

of the car, which are initially stiffer than the bracket, start to absorb significant amount of energy. Accordingly, continuing the simulations longer than 8 ms is not appropriate, because the energy absorbing capacity of the bracket is consumed.

The analysis consists of a single explicit dynamic step. In the simulations, automatic time incrementation is used with element-by-element stable time increment estimates.

4.3. Constitutive Model

Materials show an increase in their yield strength with an increase in plastic strain as well as strain rate. During a crash, the tubes severely deforms in a very short time. For this reason, a realistic simulation of a crash event requires a constitutive equation that accounts for non-linear and strain-rate dependent deformation and also work hardening. In the present FE model, Johnson - Cook constitutive model [52] is used. According to this model, the equivalent flow stress of the material, $\bar{\sigma}$, depends on equivalent plastic strain and its rate, as

$$\bar{\sigma} = \left[\bar{\sigma}_0 + B(\bar{\epsilon}^{pl})^n \right] \left[1 + C \ln \left(\frac{\dot{\bar{\epsilon}}^{pl}}{\dot{\epsilon}_0} \right) \right] \qquad (4.1)$$

Table 4.1. The basic material properties and Johnson-Cook constants for
AA6061-T6 [53].

E (GPa)	ρ (kg/m^3)	ν	A (MPa)	B (MPa)	n	C	m	D_1	D_2	D_3	D_4
70	2700	0.33	324	114	0.42	0.002	1.34	-0.77	1.45	-0.47	0.0

where $\bar{\epsilon}^{pl}$ is equivalent plastic strain, $\dot{\bar{\epsilon}}^{pl}$ is its rate, $\bar{\sigma}_0$ is the initial yield stress. The values of strain hardening coefficient, B, and exponent, n, can be obtained using quasi-static tension tests at constant strain rate. The value of the strain rate parameter, C, is determined through dynamic tension tests at varying strain rates. Note that temperature effect is excluded in the present model. The parameters for 6061-T6 aluminum alloy provided by Lesuer *et al.* [53] are given in Table 4.1.
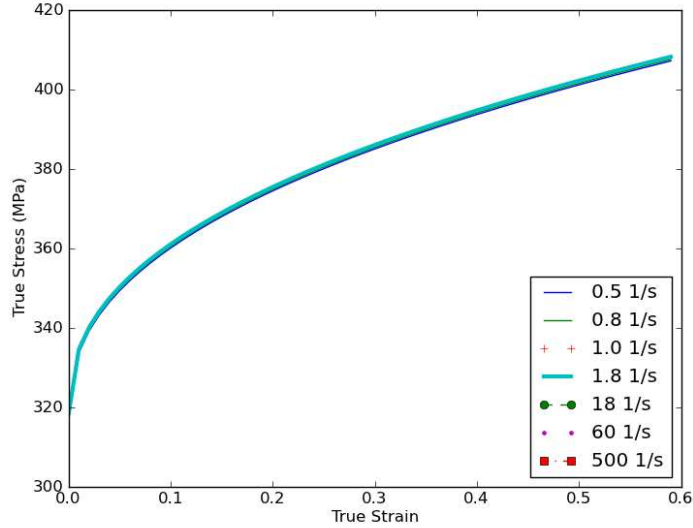
Figure 4.6. Stress-strain curves of AL 6061-T6 aluminum alloy for various strain rates.

Using the parameters which is taken from Corbett [54] *et al.* et al for AL 6061-T6 aluminum alloy, the sress-strain curves for various strain rates are plotted. As seen Figure 4.6, AL 6061-T6 aluminum alloy is almost indifferent to strain rate change.

4.4. Failure Model

Severity of the crash may result in local failures like cracks. These may affect further deformation behavior and energy absorbing capacity of the bumper. For this

reason, a cumulative failure model proposed by Johnson and Cook [55] is adopted in this study.

In the model, a critical equivalent fracture strain, $\bar{\epsilon}_f^{pl}$, is defined, which depends on hydrostatic tension, p, and effective stress, $\bar{\sigma}$. The failure strain is expressed via four material constants, $D_1 - D_4$ as

$$\bar{\epsilon}_f^{pl} = \left[D_1 + D_2 e^{D_3 \bar{\sigma}} \right] \left[1 + D_4 \ln \left(\frac{\dot{\bar{\epsilon}}^{pl}}{\dot{\epsilon}_0} \right) \right] \tag{4.2}$$

A damage parameter is defined as

$$\Omega = \frac{\bar{\epsilon}_0^{pl} + \sum \Delta \bar{\epsilon}^{pl}}{\bar{\epsilon}_f^{pl}} \tag{4.3}$$

where $\bar{\epsilon}_o^{pl}$ is the initial equivalent plastic strain and $\Delta \bar{\epsilon}^{pl}$ is an increment of the equivalent plastic strain.

As a measure of failure in finite element i, Ω_i is used, which is defined at the integration point. Failure occurs when the corresponding damage parameter, Ω_i, exceeds the unity. If failure occurs in an element, very low mechanical properties are assigned to it.

As it can be seen from the Table 4.2 the two case give very small difference, almost equal. However the one with failure model accumulates a little bit more total energy.

4.5. Meshing

Shell elements are used to model the metal sheets considering that the thickness is very small in comparison to the lateral lengths. An important question is left open is the number of integration points; full or reduced. So one has to choose element integration type out of two options which are full and reduced integrations. The expression of

"full integration" refers to the number of Gauss points required to exactly integrate the polynomial terms in an element's stiffness matrix with a regular shaped element. Fully integrated, linear elements use two integration points in each direction [56].

There is a problem in linear elements with full integration. Namely, it is shear locking. Shear locking causes the elements to be too stiff in bending. It is explained as follows. Consider a small piece of material in a structure subject to pure bending. The material will distort as shown in Figure 4.7. Lines initially parallel to the horizontal axis take on constant curvature, and lines through the thickness remain straight. The angle between the horizontal and vertical lines remains at 90^0.
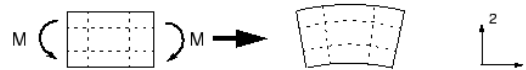
Figure 4.7. Deformation of material subjected to bending moment M [56].

The edges of a linear element are unable to curve; therefore, if the small piece of material is modelled using a single element, its deformed shape is like that shown in Figure 4.8.

Figure 4.8. Deformation of a fully integrated, linear element subjected to bending moment M [56].

Dotted lines that pass through the integration points are plotted for visualization purposes. It is obvious that the upper line has increased in length, indicating that the direct stress in the 1-direction, σ_{11}, is tensile. The length of the lower dotted line has decreased, indicating that σ_{11} is compressive. The length of the vertical dotted lines has not changed (assuming that displacements are small); therefore, σ_{22} at all integration points is zero. All this is consistent with the expected state of stress of a small piece of material subjected to pure bending. But the angle between the vertical and horizontal lines at each integration point, which was initially 90^0, has changed. This shows that the shear stress, σ_{12}, at these points is non-zero. Actually this is not correct: the shear stress in a piece of material under pure bending should be zero [56].

This artificial shear stress arises due to inability of the edges of the element to curve. Its existence means that some of the strain energy is creating shearing deformation rather than the intended bending deformation, so the overall deflections are smaller and then the element is too stiff.

Shear locking solely affects the performance of fully integrated linear elements subjected to bending loads. These elements function perfectly well under direct or shear loads. Shear locking is not an issue for quadratic elements since their edges are able to curve.

Fully integrated linear elements should be used only when it is fairly certain that the loads will produce minimal bending in your model. Using a different element type will be more appropriate if there are doubts about the type of deformation the loading will create. Fully integrated quadratic elements can also lock under complex states of stress; thus, the results should be checked carefully if they are used exclusively in the model. However, they are very useful for modeling areas where there are local stress concentrations [56].

On the other hand, reduced-integration elements use one fewer integration point in each direction than the fully integrated elements. Reduced-integration linear elements have just a single integration point located at the element's centroid [56].

Linear reduced-integration elements tend to be too flexible because they suffer from their own numerical problem called hour-glassing. Again, consider a single reduced-integration element modeling for a small piece of material subjected to pure bending (see Figure 4.9).

Figure 4.9. Deformation of a linear element with reduced integration subjected to bending moment M [56].

The length of the dotted lines, as well as the angle between them does not change,

which means that all components of strain at the element's single integration point are zero. This bending mode of deformation is thus a zero-energy mode because no strain energy is generated by this element distortion. The element is unable to resist this type of deformation since it has no stiffness in this mode. In coarse meshes this zero-energy mode can propagate through the mesh, producing meaningless results [56].

So, the analysis time by using reduced integration elements will be less than the one with full integration elements. Displacement-based FE formulations generally over-estimate the stiffness matrix and the use of fewer integration points in a element produce a less stiff element. Therefore, especially non-linear problems, it is actually advisable to use reduced integration instead of full integration.

In Abaqus, a small amount of artificial "hourglass stiffness" is introduced in first-order reduced-integration elements to limit the propagation of hourglass modes. This stiffness is more effective at limiting the hourglass modes when more elements are used in the model, which means that linear reduced-integration elements can give acceptable results as long as a reasonably fine mesh is used. The errors arising with the finer meshes of linear reduced-integration elements are within an acceptable range for many applications [56].

Integral viscoelastic approach in Abaqus/Explicit:

The integral viscoelastic approach available in Abaqus/Explicit generates more resistance to hourglass forces early in the analysis step where sudden dynamic loading is more probable.

Let q be an hourglass mode magnitude and Q be the force (or moment) conjugate to q. The integral viscoelastic approach is defined as

$$Q = \int\limits_0^t sK(t - t\prime)\frac{dq}{dt}dt\prime \qquad (4.4)$$

where K is the hourglass stiffness selected by Abaqus/Explicit, and s is one of up to three scaling factors s_s, s_r, s_w that you can define (by default, $s_s = s_r = s_w = 1.0$). The scale factors are dimensionless and relate to specific displacement degrees of freedom. For solid and membrane elements s_s scales all hourglass stiffnesses. For shell elements s_s scales the hourglass stiffnesses related to the in-plane displacement degrees of freedom, and s_r scales the hourglass stiffnesses related to the rotational degrees of freedom. In addition, s_w scales the hourglass stiffness related to the transverse displacement for small-strain shell elements [56]. In this study, the default values are used.

However, the problem with the linear reduced integration elements is, as discussed before, hour-glassing. The severity of this effect can be checked via the fraction of artificial energy to the total energy. The fraction should be so small in order to use the reduced integration elements. This issue will be addressed in latter sections.

In Table 4.3 the results are not much different from each other. However, the element with full integration gives less strain energy but higher plastic dissipation values in comparison to the results of the element with reduced integration. In total, the energies accumulated within the bumper after impact is higher for full integration elements.

By taking all these considerations into account regarding element integration, one can say linear full integration elements behave stiffer under bending loads. This trend can be seen in the Table 4.3. As an evidence, full integration elements accumulate less amount of elastic strain energy. However against this argument, one can ask if full integration elements behave stiffer in bending, should the plastic dissipation within the bumper be lower in comparison the reduced integration elements' results also? The answer is no. Because the total energy in the system is very much higher than the amount of the total energy dissipated within the bumper for both cases of integration as should be due. The elements with reduced integration reach their limits and fail enabling accumulate more energy any more. On the other hand, the full integration elements that need more energy to make them fail dissipated more energy before failure.

In the light of the late discussion, the element type used in the finite element models is S4R, a 4-node doubly curved thin or thick shell, quadrilateral, shell element with reduced integration and a large-strain formulation as shown in Figure 4.10. They account for finite membrane strains and arbitrarily large rotations; therefore, they are suitable for large-strain analysis. These elements allow transverse shear deformation. They use thick shell theory as the shell thickness increases and become discrete Kirchhoff thin shell elements as the thickness decreases; the transverse shear deformation becomes very small as the shell thickness decreases. Simpson thickness integration rule is applied using five thickness integration points.
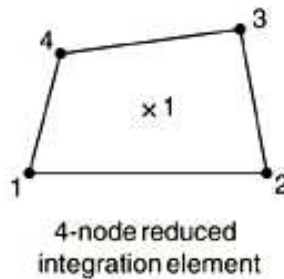
Figure 4.10. 4-node reduced integration shell element.

4.6. Contact Modeling

One of the key issues in the analysis of crash phenomena is how to simulate interacting components. The nature of this problem necessitates so many contact interactions including self contact for bumper beam and crush-boxes. So, there is a need for a contact algorithm that can accounts for all foregoing matters. "The general contact" can deal with all types of contact interaction including self contact without defining contact pairs. In comparison to the "surface-to-surface" contact this algorithm is more robust. So, the general contact algorithm was selected in order to model the contact interactions in the finite element model.

In crash-box optimization case, there is a little modification, namely, the contact between the crash-box and the rigid plate and block are modeled using surface-to-surface contact modeling. However, in order to account for self contact of the crash-box, the general contact algorithm is used in the finite element model.

In this study, the contact between the parts is modeled by finite-sliding contact with penalty contact enforcement. There are some reasons to opt for the penalty contact enforcement over kinematic contact enforcement on the location where the impact occurs. Firstly, the method of kinematic contact enforcement brings about kinetic energy losses in contacting nodes. This energy loss can be significant with a coarse mesh. Secondly, the penalty contact algorithm can model some types of contact that the kinematic contact algorithm cannot. Therefore, the penalty contact enforcement method is employed to enforce the contact compatibility between contacting surfaces.

Generally, contact constraints in a finite element model are applied in a discrete manner, meaning that for hard contact a node on one surface is constrained to not penetrate the other surface. In pure master-slave contact the node with the constraint is part of the slave surface and the surface with which it interacts is called the master surface. For balanced master-slave contact Abaqus/Explicit calculates the contact constraints twice for each set of surfaces in contact, in the form of penalty forces: once with the first surface acting as the master surface and once with the second surface acting as the master surface. The weighted average of the two corrections (or forces) is applied to the contact interaction.

Balanced master-slave contact minimizes the penetration of the contacting bodies and, thus, provides better enforcement of contact constraints and more accurate results in most cases. For this reason, balanced master-slave contact is adopted.

The finite-sliding formulation is chosen for general contact in Abaqus/Explicit. This formulation allows for arbitrary separation, sliding, and rotation of the surfaces in contact. This algorithm assumes that the incremental relative tangential motion between surfaces does not significantly exceed the dimensions of the master surface facets, but there is no limit to the overall relative motion between surfaces. It is rare for the incremental motion to exceed the facet size because of the small time increment used in explicit dynamic analyses.

4.6.1. Friction Model

When surfaces are in contact they usually transmit shear as well as normal forces across their interface. So there is a need to define the tangential and normal behavior of contacting surfaces.

The static friction coefficient corresponds to the value given at zero slip rate and the kinetic friction coefficient corresponds to the value given at the highest slip rate. The transition between static and kinetic friction is defined by the values given at intermediate slip rates.

Abaqus also provides a model to specify a static and a kinetic friction coefficient directly. In this model it is assumed that the friction coefficient decays exponentially from the static value to the kinetic value according to the formula of $\mu = \mu_k + (\mu_s - \mu_k)e^{-d_c \gamma_{eq}}$ where μ_k is the kinetic friction coefficient, μ_s is the static friction coefficient, d_c is a user-defined decay coefficient, and γ_{eq} is the slip rate. This model can be used only with isotropic friction and does not allow dependence on contact pressure, temperature, or field variables. In this study, the static friction coefficient is 0.15; the kinetic friction coefficient is 0.12; decay coefficient is 1.

Table 4.2. Energy results of bumper-beam of benchmark design using AL 6061-T6 aluminium with and without failure model.

Explanation	Elastic Energy (J)	Plastic Dissipation Energy (J)	Total Energy (J)	Standard Deviation	Mass (kg)	SEA (m^2/s^2)
w/ failure	292.2	2828.4	3120.6	581.9	2.01734	1546.8
w/o failure	293.8	2820.1	3113.9	593.2	2.01734	1543.6

Table 4.3. Energy results of bumper-beam of benchmark design using AL 6061-T6 aluminum for integration type with failure model.

Explanation	Elastic Energy (J)	Plastic Dissipation Energy (J)	Total Energy (J)	Standard Deviation	Mass (kg)	Analysis Time (min)
Rcd Int'n	292.2	2828.4	3120.6	581.9	2.01734	44
Full Int'n	285.8	2940.2	3226.0	590.2	2.01734	64

5. RESULTS AND DISCUSSION

5.1. Bumper-Beam

5.1.1. Comparison of FEM Results with a Test Case

In order to validate the accuracy of the finite element model used in the present study, the model is adapted to a similar problem and the results obtained by the FE model are compared with the experimental results. The test case is the three-point bending crash test conducted by Guo and Yu [57].
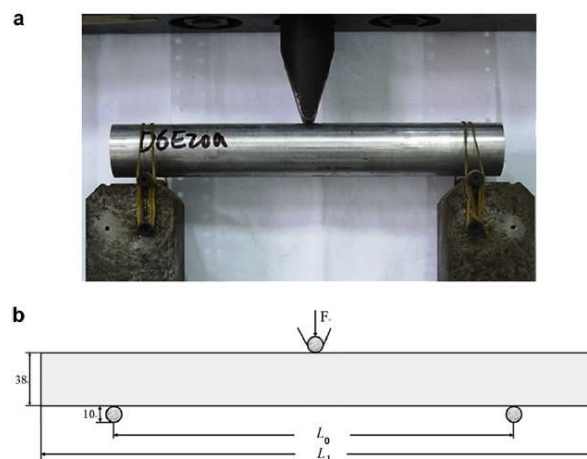
Figure 5.1. A schematic of the set-up for the dynamic three-point bending tests conducted by Guo and Yu [57].

The tests as illustrated schematically in Figure 5.1 were conducted on a drop weight testing machine. The mass of the impactor was 24.23 kg and the drop height was 141.8 cm. The initial impact energy was about 336 J. The diameters of the cylindrical punch and supports were 10 mm [57].

The test is simulated using the aforementioned procedure developed for the bumper-beam case. Figure 5.2 shows the relation between the force measured at the supports and the displacement measured at the middle. The numerical results correlate well with the experimental data as seen in the figure.
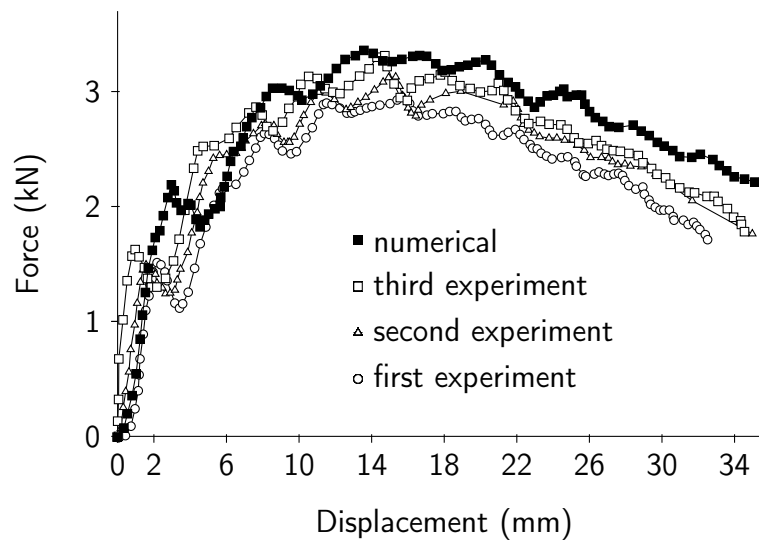
Figure 5.2. Comparison of the present FEM results with the three-point bending
impact test data [57].

5.1.2. Convergence Analysis
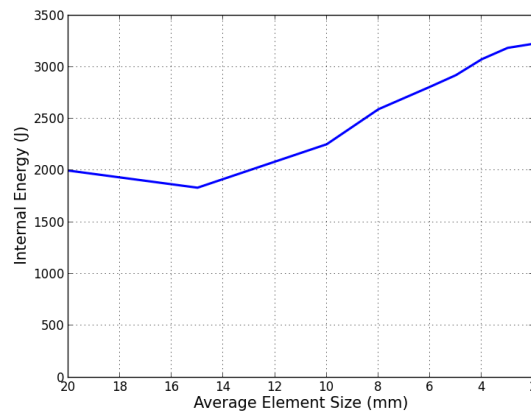
Figure 5.3. Accumulated internal energies of the bumper beam for different element
sizes.

Since the finite element method is an approximate solution technique, one should
ensure that the resulting error is less than an acceptable limit. One of the ways to check
the accuracy of the results is the mesh-convergence analysis. One should determine the
range of values for the mesh size for which consistent results are obtained. The internal
energy stored in the bumper is chosen as the control parameter in the convergence
analysis. Figure 5.3 indicates that the results converge to a value of about 3.2 kJ and
4 mm element size yields sufficiently accurate results.

5.1.3. Results

The shape optimization problem is solved for various combinations of weighting factors, w_i, in Equation 3.1. The optimal shapes obtained by the algorithm and the chosen benchmark shapes are shown in Figure 5.4 and a comparison of the results is given in Table 5.1.

OPTIMAL SHAPES			BENCHMARKS		
w1=1, w2 =0	w1=0, w2=1	w1=0.8, w2=0.2	Currently in use	Rectangle	Dome
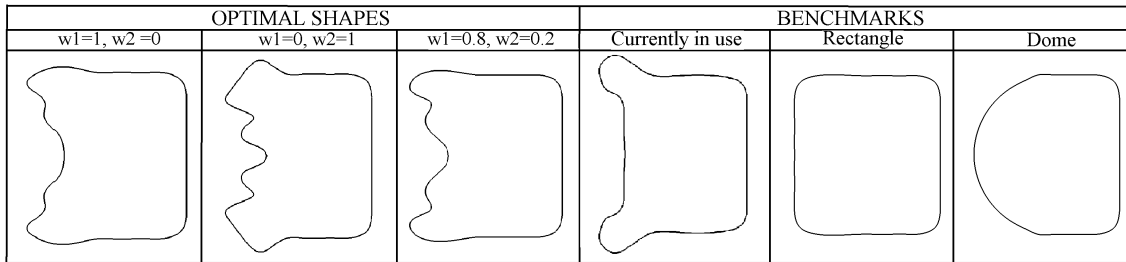
Figure 5.4. Optimal profile shapes (left three) obtained using different weighting factors and benchmark shapes (right three).

Table 5.1. Comparison of the optimal and benchmark shapes.

		Accumulated Energy (J)	Variance	Mass (kg)	Specific Energy (J/kg)
Optimal Shapes	$w_1 = 1, w_2 = 0$	3441.9	666.2	1.88	1830.8
	$w_1 = 0, w_2 = 1$	2209.4	329.1	1.97	1121.5
	$w_1 = 0.8, w_2 = 0.2$	3418.2	621.8	1.91	1789.6
Benchmarks	Currently in use	3215.3	599.9	2.03	1583.9
	Rectangle	3165.0	844.1	1.79	1768.2
	Dome	2581.6	662.4	1.63	1583.8

5.1.4. Discussion

It is noteworthy that the mass constraint ($m \leq 2.03$ kg) does not become active in the optimal shapes. In all the optimal shapes, the mass is less than that of the bumper-beam currently in use. In contrast, if one tried to increase static strength of the beam, given the spacing limitations, one would introduce deeper ribs that would increase the area moment of inertia, which would in turn increase the bending strength. On the other hand, this would also increase its rigidity and thus reduce its capacity to absorb the impact energy. In that case, the rest of the vehicle, which is represented

by the lumped parameter model in the present study, would take a significant portion of the impact energy. Too flexible beams, on the other hand, would quickly collapse. One should recognize that simple rules of thumb will not work in complex problems. The optimization algorithm finds the optimal shapes that cannot be intuitively known because of the complexity of the deformation behavior.

The optimal shaped beam that can absorb the largest strain energy is obtained using $w_1 = 1$ and $w_2 = 0$; i.e. by considering only the first term of the objective function. If only the second term is optimized, that means if the variance in the deformation is minimized ($w_1 = 0$ and $w_2 = 1$), the algorithm introduces deeper ribs to obtain more uniform deformation as seen in Figure 5.4; but the resulting shape performs poorly in absorbing impact energy. When the two terms are considered with $w_1 = 0.8$ and $w_2 = 0.2$, an interim shape is obtained (Figure 5.4).

Benchmark beams show poorer performance in terms of both energy absorbing capacity and specific energy. Among the benchmark cases, the beam with the rectangular cross-section is the best in terms of specific energy absorbing capacity; but the total energy absorbing capacity of the beam currently in use is slightly better than that of the rectangular one.

In the bumper beam, there are two critical regions, namely the region where the bumper beam is attached to the bracket (assembly region) and the region where the contact with the rigid wall ends (corner region) as shown in Figure 5.5. In the latter, a plastic hinge develops in poorly performing beams. Plastic hinge begins to form almost at the moment the car hits the wall; then the beam makes a rotation around the hinge. This occurs in beams having lower flexural stiffness like rectangular or dome-shaped beams (See Figure 5.6). Poor performance of these beams may partly be attributed to the formation of plastic hinge. As seen in Figure 5.6, the top three designs, which are the optimized ones, do not develop plastic hinges.

Figure 5.7 shows the shapes of the cross-sectional profiles in the two critical regions at various time intervals. Except for the stiff beam with minimum variance in
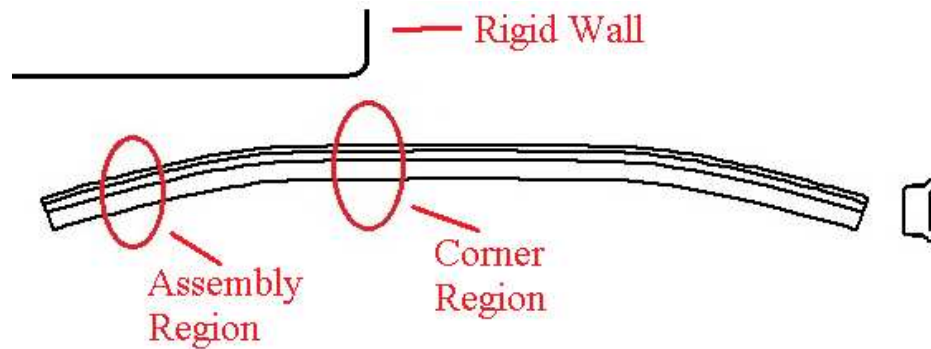
Figure 5.5. The critical regions in the bumper-beam.

deformation ($w_1 = 0$ and $w_2 = 1$), all of the beams totally collapse at the assembly region. Low stiffness beams, rectangle and dome, partially collapse in the region contacting the corner of the wall and there a plastic hinge develops.

There are other criteria that may need to be considered in bumper beam design. One such parameter is the peak force, which is the largest force at the end of the crash-box. The transmitted force can be considered as a measure of the acceleration endured by the occupants. Another is the load uniformity parameter, which is defined as the peak force divided by the mean force. In order to calculate these parameters, simulations are continued until the transmitted force makes a clear descent. The values of these parameters for the optimized and benchmark beams are given in Table 5.1. Among the optimized configurations, the one optimized with $w_{1,2} = 0, 1$ performs best according to these criteria. It is also better than the benchmark designs. These criteria may also be included in the optimization process, either in the objective function or as constraint functions; but optimization time would be longer.

Optimum design of the bumper beam for high-speed collisions increases the crash-worthiness of the vehicle, thus provides increased protection for passengers; but the bumper beams should sustain limited deformation under low-speed collisions, thus prevent damage to the remaining parts of the vehicle. This requirement could be integrated to the optimization process as a constraint. However, because additional simulations would significantly increase computational times, low-velocity requirements are not considered during optimization process. Nevertheless after obtaining the optimal shapes, they are checked whether they satisfy these requirements. For this purpose
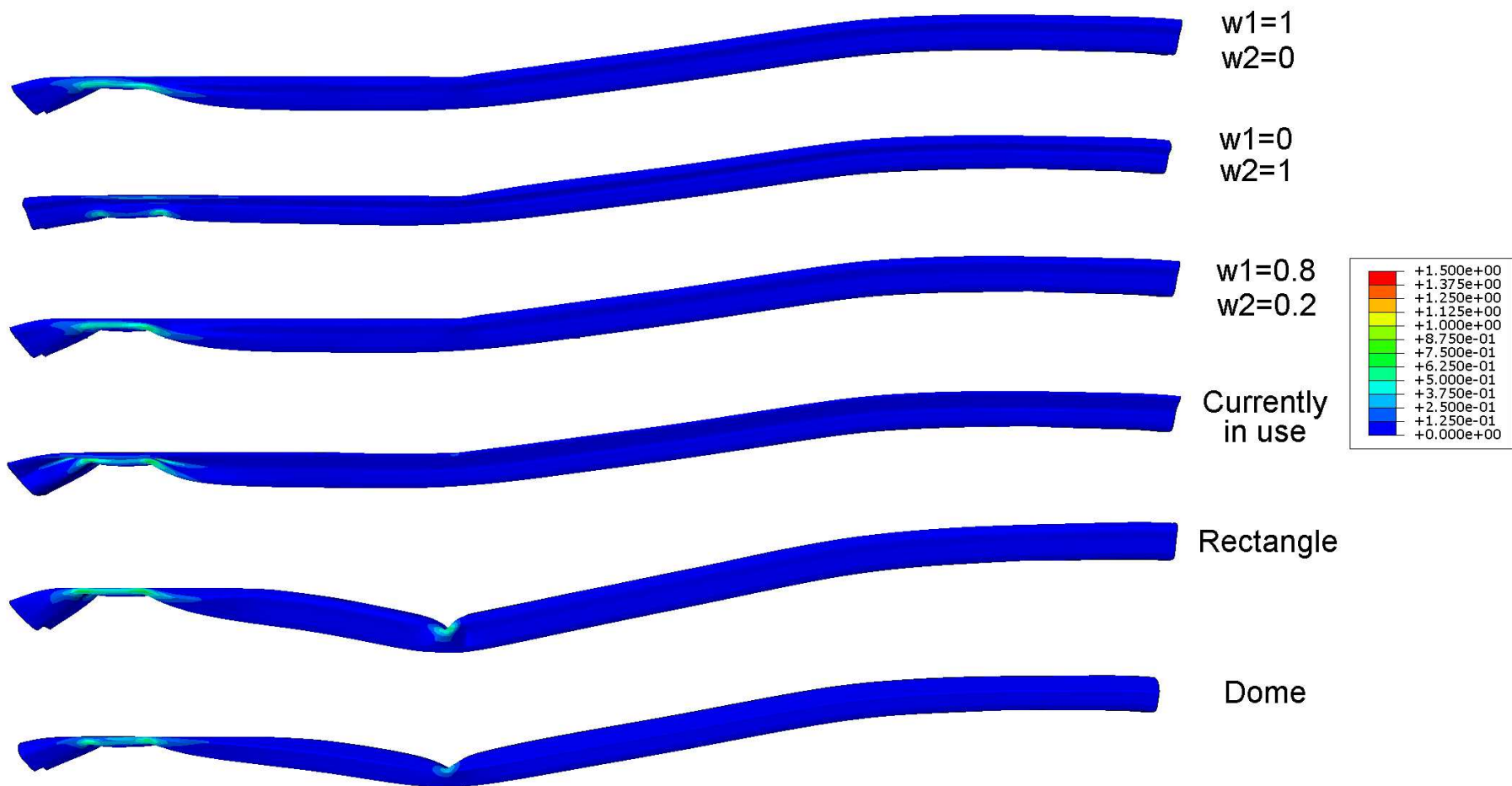
Figure 5.6. Equivalent plastic strain contour plots of bumper-beam designs after 8 ms.
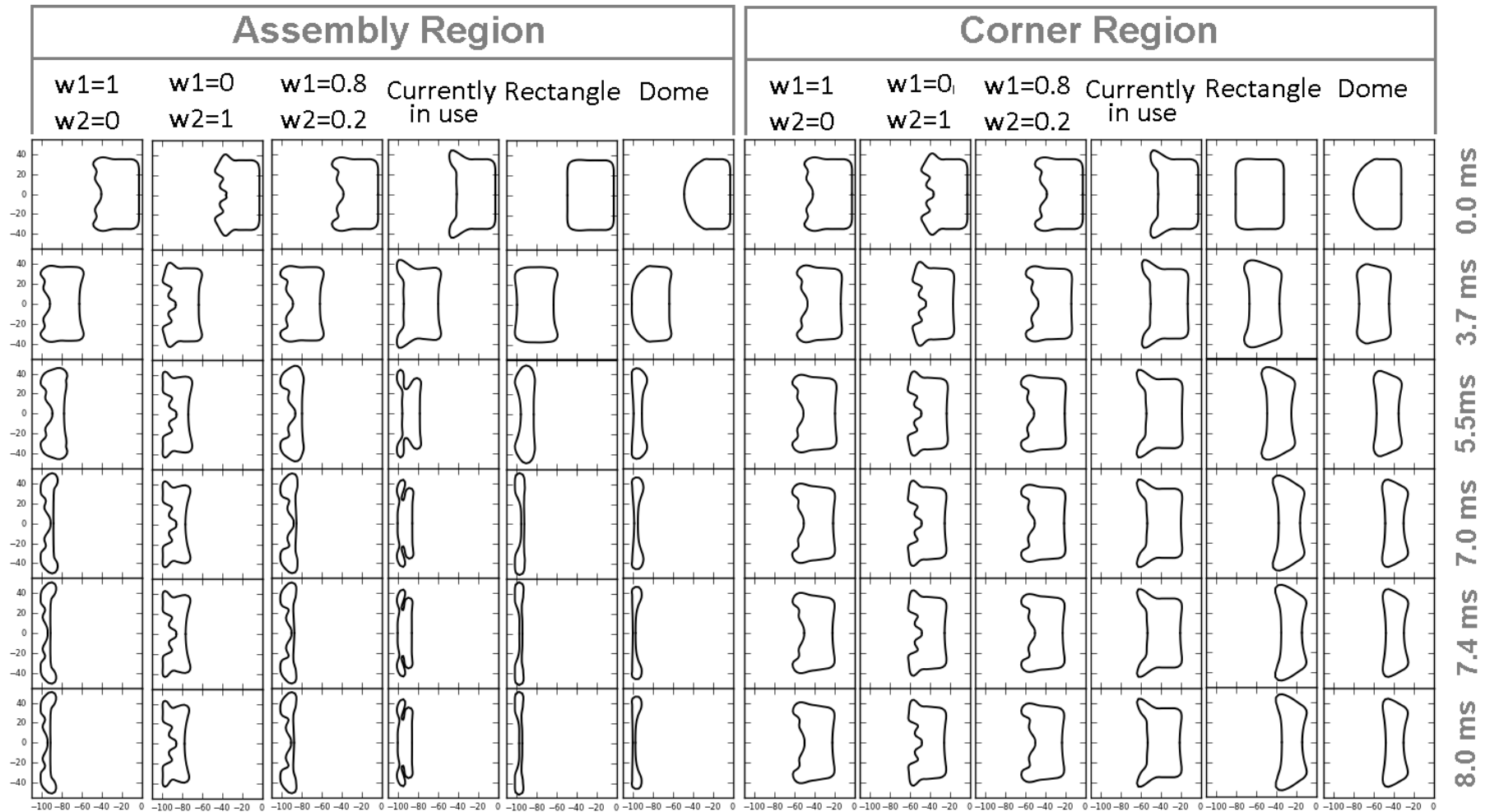
Figure 5.7. The change in the shapes of cross-sections of the assembly (left six) and corner region (right six) during crash.

three standard tests are used: the United Nations Economic Commission for Europe (ECE) Regulation No. 42, the Research Council for Automobile Repairs (RCAR) 40% offset frontal impact test, and RCAR full frontal impact test. The results of the simulations are presented in Table 5.2.

Table 5.2. Simulation results for low-velocity impact tests.

		Pendulum	RCAR Offset Test	RCAR Full Test	
		Plastically Dissipated Energy (J)	Accumulated Energy (J)	Intrusion (mm)	Deflection (mm)
Optimal Shapes	$w_{1,2} = 1, 0$	113.1	2823.2	1.735	90.175
	$w_{1,2} = 0, 1$	120.7	1586.9	1.242	83.421
	$w_{1,2} = 0.8, 0.2$	111.8	2786.2	1.783	89.102
Bench-marks	Currently in use	115.2	2418.7	2.363	95.515
	Rectangle	129	2823.5	24.368	138.029
	Dome	141.6	2017.5	1.731	85.079

In the pendulum test, a pendulum having a mass equivalent to the car's mass hits the car with velocity of 4 km/h. The smaller is the permanent deformation, the better is the crash performance. In the RCAR offset frontal test, the car with a velocity of 16 km/h hits a rigid wall with an offset. In this test, the damage to the other parts of the car should be minimal; but due to the lack of data, the absorbed energies are compared. In the RCAR full frontal test, the car hits a curved rigid wall with a velocity of 10 km/h, and the intrusion, which is defined as the difference between the displacements of the middle foremost point of the bumper beam and the back end of the crash-box, and the deflection, which is defined as the difference between the displacements of the middle back side of the bumper beam and the back end of the crash-box, are measured. Table 5.2 shows that the two configurations obtained using $w_{1,2} = 1, 0$ and $w_{1,2} = 0.8, 0.2$ are better for every single criteria than the one currently in-use and better for almost all criteria for the other two benchmark shapes. So, it can be said that optimally designing the bumper beam for the EuroNCAP offset frontal impact test results in a bumper design that is also resistant to crashes at low speeds.
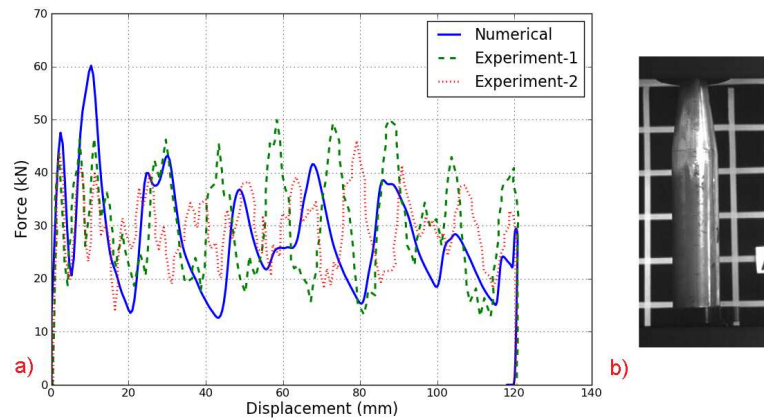
Figure 5.8. Comparison of FEM results (a) with the experimental drop test (b) data [21].

5.2. Crash-box

5.2.1. Comparison of FEM Results with a Test Case

In order to validate the accuracy of the finite element model used in the present study, the model is adapted to a similar problem and the results obtained by the FE model are compared with the experimental results obtained by Avalle and Chiandussi [21]. The tests were conducted on a drop weight testing machine in which an object was dropped on a thin-walled tube with tapered tip at rest. The mass of the hammer was 60 kg and its initial velocity was 10 m/s.

The test is simulated using the aforementioned approach with an element size of 2.0 mm. Figure 5.8 shows the relation between the force measured at the supports and the displacement measured. The numerical results correlate well with the experimental data as seen in Figure 5.8.

5.2.2. Results of Crash-Box Optimization

The shape optimization problem is solved using various combinations of weighting factors, w_i, in Equation 3.3; either only one term in the objective function is used or more than one term; that means single and multi-objective optimizations are carried

out. For single objective optimizations, the energy and mass constraints are not used. The optimization process is repeated for a constant thickness of 2.5 and 2.0 mm as well as variable thickness. The optimal shapes obtained by the algorithm and the optimal values of the optimization variables are given in Tables 5.3 and 5.4. Table 5.5 provides the results for the circular benchmark design. A comparison of the results for the optimum shapes as well as the chosen benchmark shapes is given in Table 5.6 in terms of the normalized values. Table 5.7 shows the deformation of the optimal crash-boxes during the course of collision.

It is noteworthy that the mass constraint ($m \leq 156$ g) and the total energy constraint ($\bar{E}_{acc} \geq 6672$ J) do not become active in the multi-objective optimizations. In the single-objective optimizations, where the mass and energy constraints are not imposed, the masses of the optimal designs are also less than that of the circular crash-box. In contrast, if one tried to increase the static strength of the column, given the spacing limitations, one would increase the cross-sectional area, which would in turn decrease the stress. However, this would also increase its rigidity and thus reduce its capacity to absorb impact energy. In that case, the rest of the vehicle, which is represented by the lumped-parameter model in the present study, would take a significant portion of the impact energy. Too flexible columns, on the other hand, would quickly collapse and thus its energy absorbing capacity would be quickly consumed. One should recognize that simple rules of thumb will not work in complex problems. The optimization algorithm finds the optimal shapes that cannot be intuitively known because of the complexity of the deformation behavior.

The optimal shaped tube that can absorb the largest strain energy per unit mass is obtained if only the first term of the objective function is considered i.e. $w_1 = 1$, $w_2 = 0$, and $w_3 = 0$. Even though, in these runs, the third term, F_{max}, and $\Delta F_{max}/\Delta t$, is not considered, the resulting values are much better than that of the benchmark case. If only the second term is optimized, that means if the variance in the deformation is minimized ($w_1 = 0$, $w_2 = 1$ and $w_3 = 0$), unacceptably low specific energy values are obtained. If the third term in Equation 3.3 is minimized ($w_1 = 0$, $w_2 = 0$, and $w_3 = 1$), the algorithm typically chooses larger taper angles and deeper circumferential

Table 5.3. Optimum base shapes of the crash-box for AL 6061-T6.
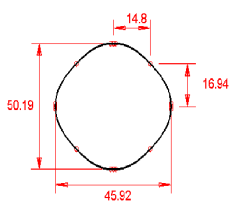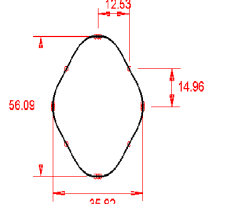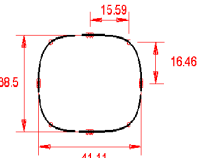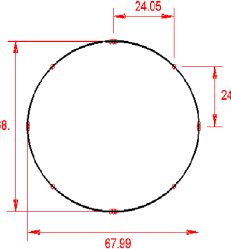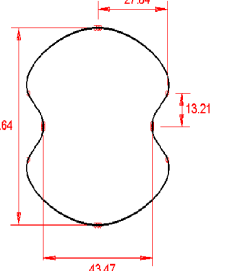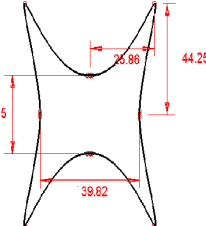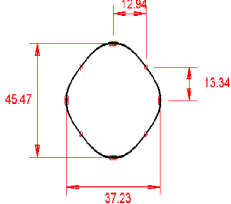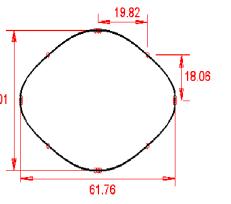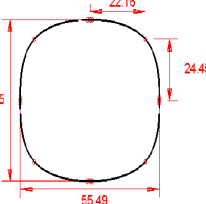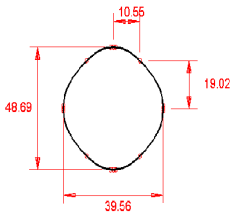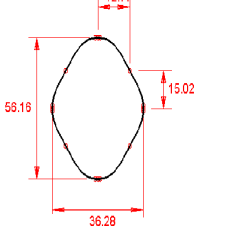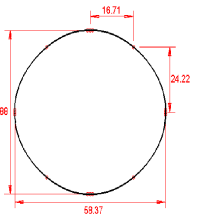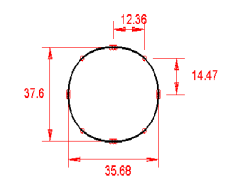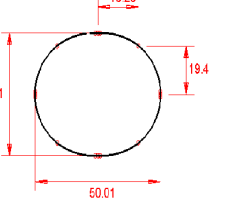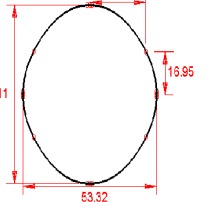
	$t = 2.5$ mm	$t = 2.0$ mm	Variable t
$w_{1,2,3} = 1, 0, 0$	14.8; 16.94; 50.19; 45.92	12.53; 14.96; 56.09; 35.82	15.59; 16.46; 38.5; 41.11
$w_{1,2,3} = 0, 1, 0$	24.05; 24; 68.; 67.99	27.84; 13.21; 78.64; 43.47	25.86; 44.25; 31.15; 39.82
$w_{1,2,3} = 0, 0, 1$	12.94; 13.34; 45.47; 37.23	19.82; 18.06; 56.01; 61.76	22.16; 24.45; 64.55; 55.49
$w_{1,2,3} = 0.5, 0.1, 0.4$	10.55; 19.02; 48.69; 39.56	12.77; 15.02; 58.16; 36.28	16.71; 24.22; 60.86; 58.37
$w_{1,2,3} = 0.5, 0, 0.5$	12.36; 14.47; 37.6; 35.68	16.26; 19.4; 49.21; 50.01	22.51; 16.95; 71.11; 53.32

Table 5.4. Optimal values of the optimization variables defining the longitudinal profile.

		c_α	r_1	r_2	r_3	l_1 (mm)	l_2 (mm)	l_3 (mm)	t (mm)
$t = 2.5$ mm	$w_{1,2,3} = 1, 0, 0$	0.849	0.929	1.008	0.892	18.941	20.466	11.248	2.5
	$w_{1,2,3} = 0, 1, 0$	1.000	1.000	1.000	1.001	17.656	29.256	28.824	2.5
	$w_{1,2,3} = 0, 0, 1$	1.084	0.968	1.106	0.941	20.539	7.989	24.357	2.5
	$w_{1,2,3} = 0.5, 0.1, 0.4$	1.015	1.031	1.069	0.990	14.333	13.253	20.954	2.5
	$w_{1,2,3} = 0.5, 0.0, 0.5$	0.850	1.051	0.888	0.919	22.968	16.530	16.693	2.5
$t = 2.0$ mm	$w_{1,2,3} = 1, 0, 0$	1.094	1.015	0.974	1.034	13.187	13.095	17.853	2.0
	$w_{1,2,3} = 0, 1, 0$	1.081	1.014	1.101	0.897	24.402	8.546	9.028	2.0
	$w_{1,2,3} = 0, 0, 1$	0.759	0.836	1.018	1.034	11.103	25.235	20.343	2.0
	$w_{1,2,3} = 0.5, 0.1, 0.4$	1.086	1.016	0.972	1.036	13.506	13.428	17.512	2.0
	$w_{1,2,3} = 0.5, 0.0, 0.5$	1.012	0.855	0.997	1.021	16.123	19.492	8.861	2.0
Variable Thickness	$w_{1,2,3} = 1, 0, 0$	0.795	0.944	0.841	1.011	22.936	11.752	19.472	1.722
	$w_{1,2,3} = 0, 1, 0$	1.049	0.868	0.949	0.852	19.928	10.569	21.808	1.093
	$w_{1,2,3} = 0, 0, 1$	0.789	0.890	0.829	0.989	14.851	12.520	17.888	1.056
	$w_{1,2,3} = 0.5, 0.1, 0.4$	0.953	0.987	0.977	1.041	16.897	28.623	25.752	2.6
	$w_{1,2,3} = 0.5, 0.0, 0.5$	0.752	1.048	1.053	0.898	15.531	16.991	18.414	1.987
Bench marks	Circular ($D = 70$)	1.0	1.0	1.0	1.0				2.5
	Rectangular (70x100)	1.0	1.0	1.0	1.0				2.5
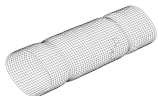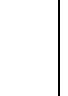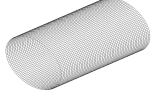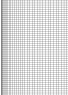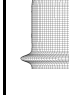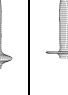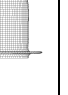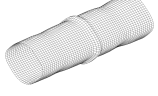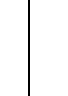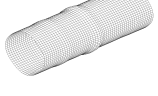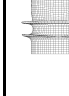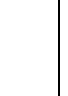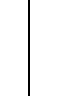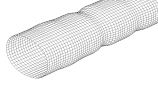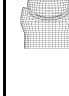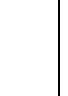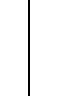
Table 5.5. Results for the circular benchmark design.
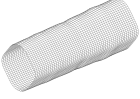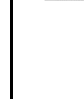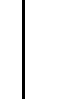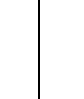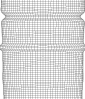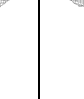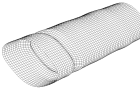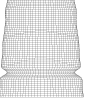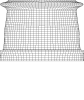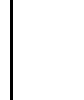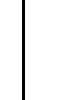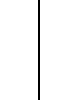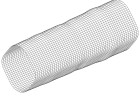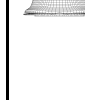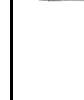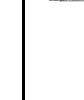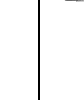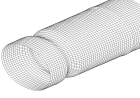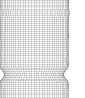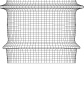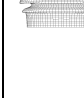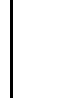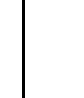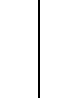
	Specific Energy (J/g)	Variance	F_{max} (kN)	$\Delta F_{max}/\Delta t$ (MN/s)	Mass (g)	Accumulated Energy (J)
Circular ($D = 70$)	39.8	900	117.2	569.3	156	6205.8
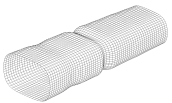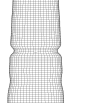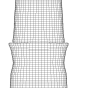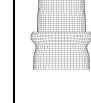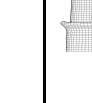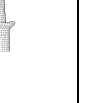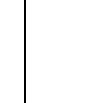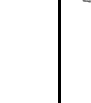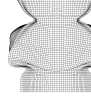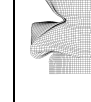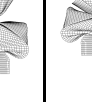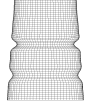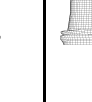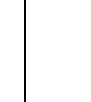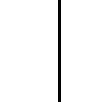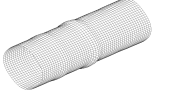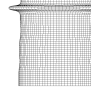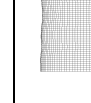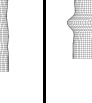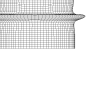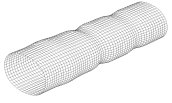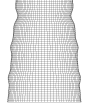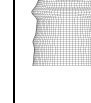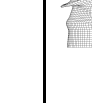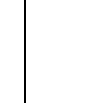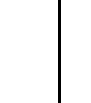
Table 5.6. Comparison of the optimal and benchmark shapes in terms of normalized values.
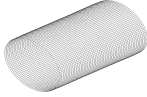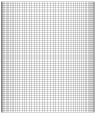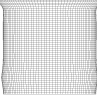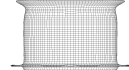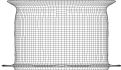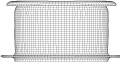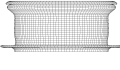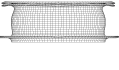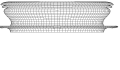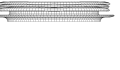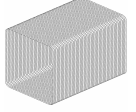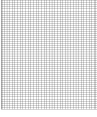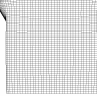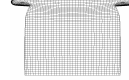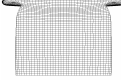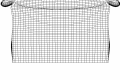
		Specific Energy	Variance	F_{max}	$\frac{\Delta F_{max}}{\Delta t}$	Mass	Accumulated Energy
$t = 2.5$ mm	$w_{1,2,3} = 1, 0, 0$	2.18	2.45	0.47	0.44	0.64	1.40
	$w_{1,2,3} = 0, 1, 0$	1.00	0.98	1.00	1.00	1.00	1.00
	$w_{1,2,3} = 0, 0, 1$	1.57	2.04	0.48	0.20	0.62	0.97
	$w_{1,2,3} = 0.5, 0.1, 0.4$	2.14	2.16	0.64	0.45	0.64	1.37
	$w_{1,2,3} = 0.5, 0.0, 0.5$	2.05	5.78	0.45	0.38	0.62	1.26
$t = 2.0$ mm	$w_{1,2,3} = 1, 0, 0$	2.26	2.82	0.56	0.42	0.56	1.28
	$w_{1,2,3} = 0, 1, 0$	1.07	0.95	0.52	0.33	0.95	1.02
	$w_{1,2,3} = 0, 0, 1$	1.65	1.91	0.30	0.12	0.62	1.02
	$w_{1,2,3} = 0.5, 0.1, 0.4$	2.08	2.69	0.54	0.41	0.56	1.17
	$w_{1,2,3} = 0.5, 0.0, 0.5$	2.02	3.40	0.34	0.25	0.59	1.19
Variable Thickness	$w_{1,2,3} = 1, 0, 0$	2.91	3.75	0.22	0.17	0.38	1.12
	$w_{1,2,3} = 0, 1, 0$	0.90	0.59	0.30	0.23	0.69	0.62
	$w_{1,2,3} = 0, 0, 1$	2.19	0.81	0.09	0.04	0.36	0.79
	$w_{1,2,3} = 0.5, 0.1, 0.4$	1.38	2.87	0.90	0.70	0.90	1.24
	$w_{1,2,3} = 0.5, 0.0, 0.5$	2.83	3.65	0.22	0.18	0.38	1.09
Bench marks	Circular ($D = 70$)	1.0	1.0	1.0	1.0	1.0	1.0
	Rectangular (70x100)	0.66	1.60	0.63	0.62	1.54	1.01

Table 5.7. Comparison of the deformed shapes.

$w_{1,2,3} =$	3D	0.00 s	0.001 s	0.002 s	0.003 s	0.004 s	0.005 s	0.006 s	0.007 s	0.008 s
$1, 0, 0$										
$0, 1, 0$										
$0, 0, 1$										
$0.5, 0.1, 0.4$										
$0.5, 0.0, 0.5$										

$t = 2.5$ mm

$w_{1,2,3} =$	3D	0.00 s	0.001 s	0.002 s	0.003 s	0.004 s	0.005 s	0.006 s	0.007 s	0.008 s
$1, 0, 0$										
$0, 1, 0$										
$0, 0, 1$										
$0.5, 0.1, 0.4$										
$0.5, 0.0, 0.5$										

$t = 2.0$ mm

$w_{1,2,3} =$	3D	0.00 s	0.001 s	0.002 s	0.003 s	0.004 s	0.005 s	0.006 s	0.007 s	0.008 s
$1, 0, 0$										
$0, 1, 0$										
$0, 0, 1$										
$0.5, 0.1, 0.4$										
$0.5, 0.0, 0.5$										

Variable Thickness

$w_{1,2,3} =$	3D	0.00 s	0.001 s	0.002 s	0.003 s	0.004 s	0.005 s	0.006 s	0.007 s	0.008 s
Benchmarks Circular										
Rectangular										

ribs to minimize the jerk effect; interestingly specific energy absorption is also improved together with total accumulated energy, though the later is not as good as the former. When the three terms are considered with $w_1 = 0.5$, $w_2 = 0.1$, and $w_3 = 0.4$, more balanced results are obtained (Table 5.3 and 5.7). Recognizing that the contribution of low variance in deformation to crashworthiness is questionable, the crash-box is optimized considering only the first and the third terms ($w_1 = 0.5$, $w_2 = 0$ and $w_3 = 0.5$). For this case, F_{max} and $\Delta F_{max}/\Delta t$ values are improved in comparison to the first case ($w_1 = 1$, $w_2 = 0$ and $w_3 = 0$). The crash-box designs with optimized thickness outperform the corresponding designs optimized using the same weights but with a predefined thickness.

5.3. Assembly

So far, the performances of bumper-beam and the crash-box are evaluated individually. However, optimization of individual parts may not lead to better results for the system as a whole. For this end, the two selected components, namely the optimal bumper-beam obtained with $w_{1,2} = 1, 0$ and the optimal crash-box obtained with $w_{1,2,3} = 0.5, 0.1, 0.4$ and variable thickness, are assembled and tested according to foregoing tests.

The selected optimal design of the crash-box is not suitable for assembly with the bumper-beam. Therefore, some subparts are added as shown in Figures 5.9 and 5.10.

The assembly is shown in Figure 5.11

The comparison of the results obtained with the optimal design and the design currently-in-use are given in Tables 5.8-5.11. In these tables, the data are provided for the bumper-beam - crash-box assembly. Also, the plastic equivalent strain contour plots of the two designs are depicted in Figures 5.13-5.15.

Here, EuroNCAP test is simulated for a time duration 2 ms longer in comparison to the bumper-beam optimization case in order to let the deformation of the crash-box

reach its maturity.

Table 5.8. Comparison of the assemblies of the optimal and benchmark shapes for EuroNCAP test.

	Accumulated Energy (J)	Mass (kg)	Specific Energy (J/kg)	Peak Force (kN)	Load Uniformity
Optimal Design	9429.9	2.67	3531.8	83.5	2.17
Currently-in-use	7579.9	2.82	2687.9	88.0	2.47

Table 5.9. Simulation results for ECE pendulum impact tests.

	Plastically Dissipated Energy (J)
Optimal Design	106.3
Currently in use	115.2

Table 5.10. Simulation results for low-velocity impact tests for RCAR oblique test.

	Accumulated Energy (J)
Optimal Design	8284.9
Currently in use	6784.6

Table 5.11. Simulation results for low-velocity impact tests of RCAR full frontal impact test.

	Intrusion (mm)	Deflection (mm)
Optimal Design	2.068	92.620
Currently in use	2.363	95.515

Table 5.8- 5.11 show that the combination of selected two configurations is better than the combination of currently in-use bumper-beam and crash-box for every single criteria.
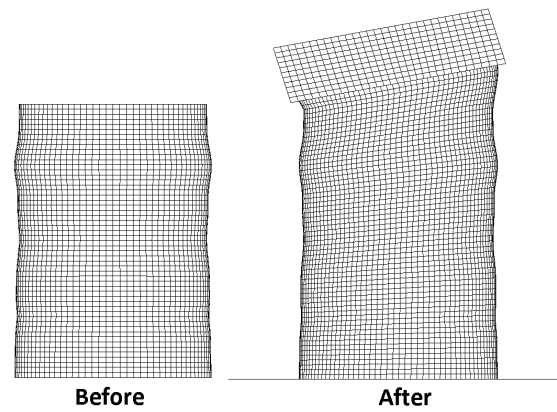
Figure 5.9. Meshed depictions of the crash-box (a), and its assembly version (b).
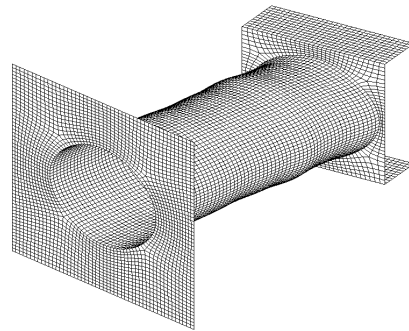
Figure 5.10. A meshed depiction of the selected optimal design of crash-box for
assembly.
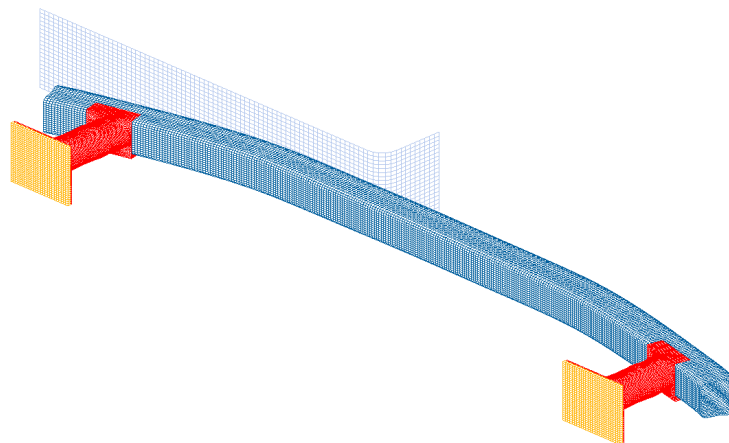
Figure 5.11. A meshed depiction of the assembled optimal designs, the bumper-beam
obtained with $w_{1,2} = 1, 0$ and the crash-box obtained with $w_{1,2,3} = 0.5, 0.1, 0.4$ and
variable thickness, for EuroNCAP offset frontal test.
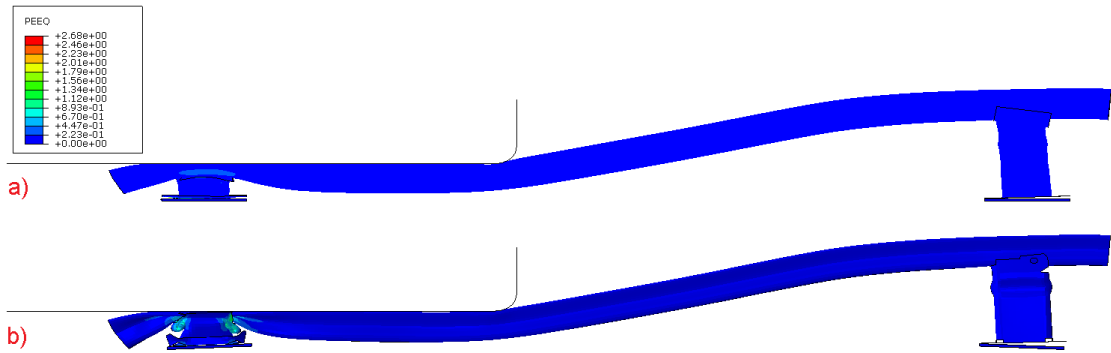
Figure 5.12. Plastic equivalent strain contour plots of (a) optimal design (b) currently-in-use at the end of the analysis for EuroNCAP offset frontal test.
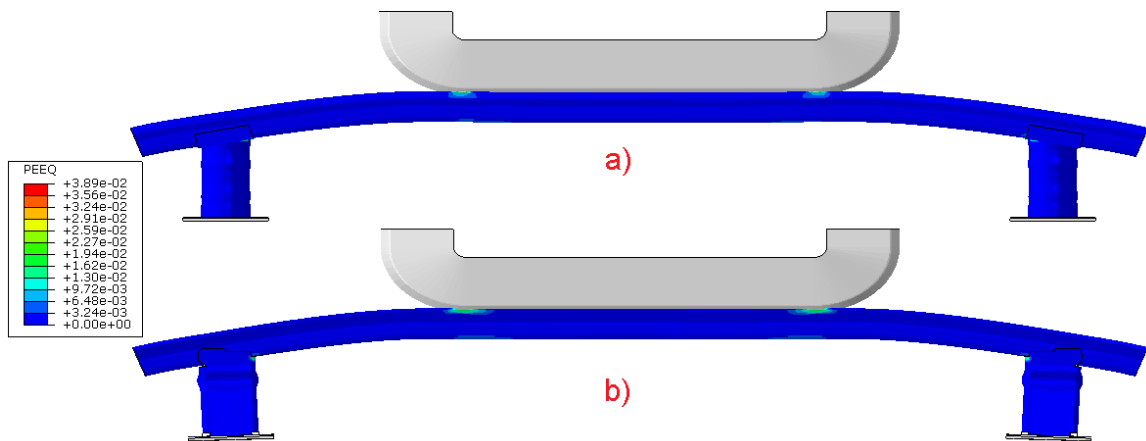
Figure 5.13. Plastic equivalent strain contour plots of (a)) the optimal design (b) currently-in-use at the end of the analysis for ECE Pendulum test.
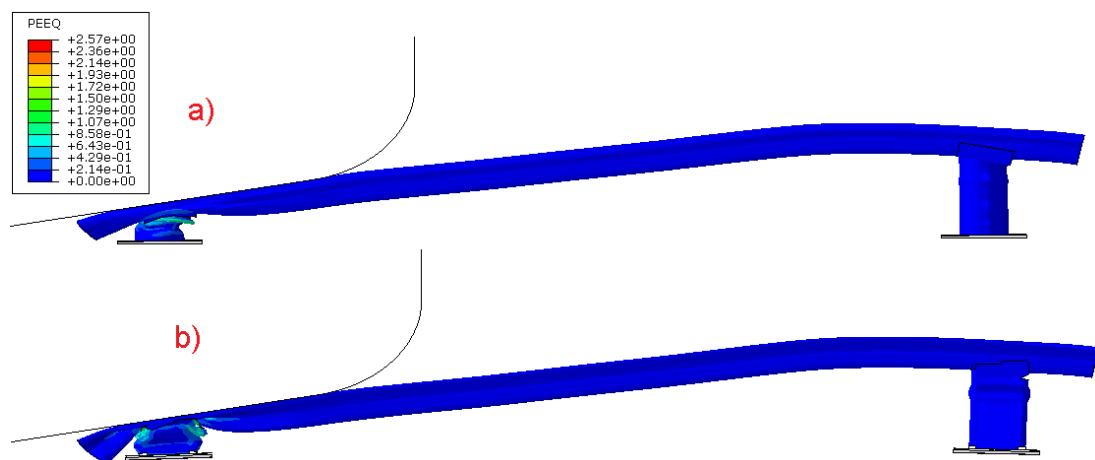
Figure 5.14. Plastic equivalent strain contour plots of (a)the optimal design (b) currently-in-use at the end of the analysis for RCAR offset frontal test.
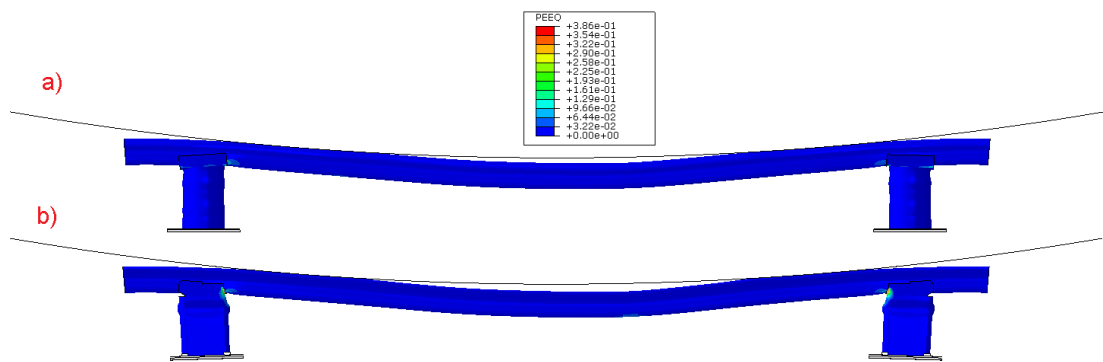
Figure 5.15. Plastic equivalent strain contour plots of (a) the optimal design (b) currently-in-use at the end of the analysis for RCAR full frontal test.

6. AN ANALYTICAL APPROXIMATE MODEL FOR THE BUMPER-BEAM AND THE CRASH-BOX

In this section, EuroNCAP test results for the optimal design is compared with those of an analytical model developed in this thesis.

6.1. Assumptions

- The beam is considered as straight.
- The masses of the beam and spring are neglected.
- The beam and the springs respond elastically.
- The beam is modeled as Euler-Bernoulli beam.
- The distribution of the load is not found by analysis but presumed.
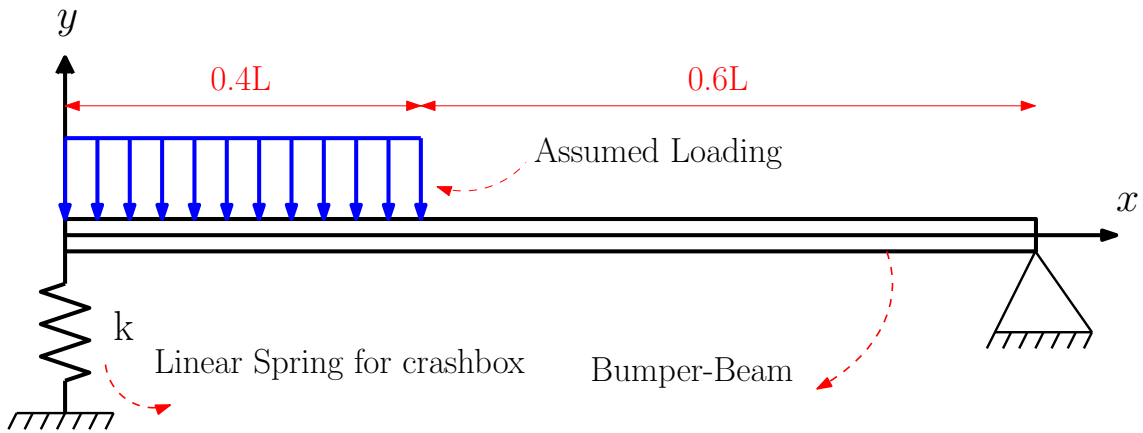
Figure 6.1. The analytical model of the bumper-beam.

6.2. Inputs

- E : Elastic modulus of the material the bumper-beam is made of
- I : Area moment of inertia, which should be supplied for a new design
- L : Length of the beam, which should be supplied for a new design
- k : Stiffness of the beam, which should be input for a different crash-box
- U : Strain energy absorbed by the bar and the spring

Displacement of the beam, at the time of maximum deflection is $u = u(x)$. The

corresponding strain energy can be split up into two components:

$$U = U_b + U_s \tag{6.1}$$

where U_b is the energy absorbed by the beam, U_s is the energy absorbed by the spring

$$U_b = \int_0^L \frac{EI}{2} \left(\frac{d^2u}{dx^2} \right)^2 dx = \int_0^L \frac{M^2}{2EI} \tag{6.2}$$

$$U_s = \frac{1}{2} k u(0)^2 \tag{6.3}$$

Let us find the form of $u(x)$ corresponding to the form of the distributed load $w(x)$. It is assumed that the loading is uniform and it covers 40 % of its length.
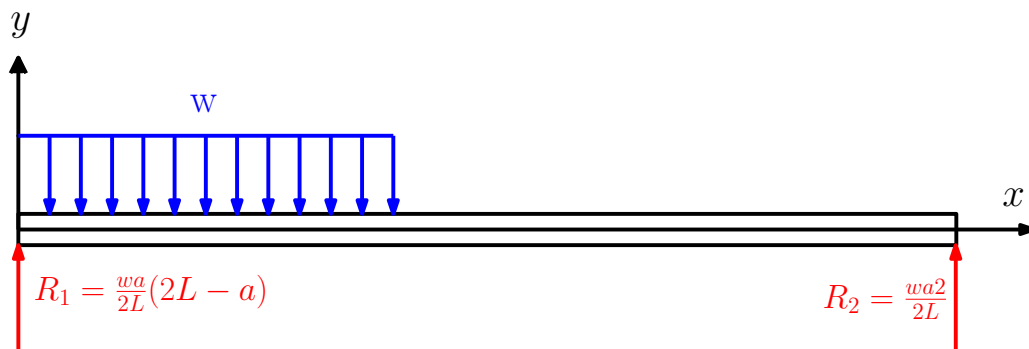
Figure 6.2. The reaction forces.

Then the moment distribution throughout the beam will be

$$M_1 = R_1 x - \frac{wx^2}{2} \; for \; 0 < x < a \tag{6.4}$$

$$M_2 = R_2(L - x) \; for \; a < x < L \tag{6.5}$$

Let us find the deflections

$$\frac{\partial^2 u_1}{\partial x^2} = \frac{M_1}{EI} = \frac{1}{EI}(R_1 x - \frac{wx^2}{2}) \ for \ 0 < x < a \tag{6.6}$$

Integrating once, we obtain

$$\frac{\partial u_1}{\partial x} = \frac{1}{EI}(\frac{R_1 x^2}{2} - \frac{wx^3}{6}) + c_1 \ for \ 0 < x < a \tag{6.7}$$

Integrating twice, we obtain

$$u_1 = \frac{1}{EI}(\frac{R_1 x^3}{6} - \frac{wx^4}{24}) + c_1 x + c_2 \ for \ 0 < x < a \tag{6.8}$$

Boundary condition

$$u(x = 0) = \frac{R_1}{k} \implies c_2 = \frac{R_1}{k} \tag{6.9}$$

$$\frac{\partial^2 u_2}{\partial x^2} = \frac{M_2}{EI} = \frac{1}{EI}(R_2(L - x)) \ for \ a < x < L \tag{6.10}$$

Integrating once, we obtain

$$\frac{\partial u_2}{\partial x} = \frac{R_2}{EI}(Lx - \frac{x^2}{2}) + c_3 \ for \ a < x < L \tag{6.11}$$

Integrating twice, we obtain

$$u_2 = \frac{R_2}{EI}(L\frac{x^2}{2} - \frac{x^3}{6}) + c_3 x + c_4 \ for \ a < x < L \tag{6.12}$$

Boundary condition

$$u(x = L) = 0 \implies \frac{R_2}{EI}(\frac{L^3}{2} - \frac{L^3}{6}) + c_3 L + c_4 = \frac{R_2}{EI}\frac{L^3}{3} + c_3 L + c_4 = 0 \qquad (6.13)$$

$$c_4 = -\frac{R_2}{EI}\frac{L^3}{3} - c_3 L \qquad (6.14)$$

The continuity condition at $x = a$

$$u_1(x = a) = u_2(x = a) \qquad (6.15)$$

$$\frac{\partial}{\partial x}u_1(x = a) = \frac{\partial}{\partial x}u_2(x = a) \qquad (6.16)$$

$$\frac{1}{EI}(\frac{R_1 a^3}{6} - \frac{wa^4}{24}) + c_1 a + \frac{R_1}{k} = \frac{R_2}{EI}(L\frac{a^2}{2} - \frac{a^3}{6}) + c_3 a - \frac{R_2}{EI}\frac{L^3}{3} - c_3 L \qquad (6.17)$$

$$\frac{1}{EI}\left(\frac{R_1 a^2}{2} - \frac{wa^3}{6}\right) + c_1 = \frac{R_2}{EI}\left(La - \frac{a^2}{2}\right) + c_3 \qquad (6.18)$$

$$\begin{bmatrix} a & L-a \\ 1 & -1 \end{bmatrix} \begin{bmatrix} c_1 \\ c_3 \end{bmatrix} = \begin{bmatrix} -\frac{1}{EI}(\frac{R_1 a^3}{6} - \frac{wa^4}{24}) - \frac{R_1}{k} + \frac{R_2}{EI}(L\frac{a^2}{2} - \frac{a^3}{6}) - \frac{R_2}{EI}\frac{L^3}{3} \\ -\frac{1}{EI}\left(\frac{R_1 a^2}{2} - \frac{wa^3}{6}\right) + \frac{R_2}{EI}\left(La - \frac{a^2}{2}\right) \end{bmatrix} \qquad (6.19)$$

$$c_1 = -\frac{aw(2L - a)(2kL^2 a - kLa^2 + 12EI)}{24EIL^2 k} \qquad (6.20)$$

$$c_3 = -\frac{aw(4kL^3 a + kLa^3 + 24EIL - 12EIa)}{24EIL^2 k} \qquad (6.21)$$

So, the displacement becomes

$$u(x_1) = \begin{cases} \frac{1}{EI}(\frac{R_1 x^3}{6} - \frac{wx^4}{24}) - \left(\frac{aw(2L-a)(2kL^2a-kLa^2+12EI)}{24EIL^2k}\right)x + \frac{R_1}{k} & \text{for } 0 \le x_1 \le a \\ \frac{R_2}{EI}(\frac{Lx^2}{2} - \frac{x^3}{6}) - \frac{aw(4kL^3a+kLa^3+24EIL-12EIa)}{24EIL^2k}x - \frac{R_2L^3}{3EI} + \frac{awL(4kL^3a+kLa^3+24EIL-12EIa)}{24EIL^2k} & \text{for } a \le x_1 \le L \end{cases}$$

$$(6.22)$$

$$U = \int_0^a \frac{M_1^2}{2EI} + \int_a^L \frac{M_2^2}{2EI} + \frac{1}{2}ku(0) \tag{6.23}$$

$$U = \int_0^a \frac{R_1^2 x^2 - R_1 wx^3 + \frac{w^2 x^4}{4}}{2EI} + \int_a^L \frac{R_2^2(L^2 - 2Lx + x^2)}{2EI} + \frac{1}{2}ku(0) \tag{6.24}$$

$$U = \frac{\frac{R_1^2 x^3}{3} - \frac{R_1 wx^4}{4} + \frac{w^2 x^5}{20}}{2EI}\Big|_0^a + \frac{R_2^2(L^2 x - Lx^2 + \frac{x^3}{3})}{2EI}\Big|_a^L + \frac{1}{2}ku(0)^2 \tag{6.25}$$

6.3. Calculation of the Stiffness of the Linear Spring

The crash-box located at left-hand-side of the assembly is modeled using a linear spring. To find the stiffness of the crash-box, finite element results of the crash-box optimized for EuroNCAP test are considered. According to them, the crash-box accumulated 6215.9 J of strain energy with the displacement of 104.591 mm. The energy stored by a linear spring is

$$U_s = \frac{1}{2}ku^2 \implies 6215.9 = \frac{1}{2}k0.1046^2 \implies k \simeq 113.6kN/m \tag{6.26}$$

6.4. Calculation of the Effective Young's Modulus

As stated above, the Young'âĂŹs modulus of the beam, E, is used in the calculations. However, this constant is valid for only elastic loading yet the loading makes the beam extend beyond the elastic limit. So, if Young'âĂŹs modulus is used in the calculations, it is apparent that the model will give underestimated results in terms of deformation. Therefore, an effective Young'âĂŹs modulus should be introduced for calculations. To do so, the displacement and energy absorption data produced by the finite element model can be used. That is, given the displacement data, an energy is calculated by Euler-Bernoulli beam theory. By equating these two energies, one from finite element and the other from analytical calculations, the effective Young's modulus can be found.

The finite element analysis give displacement results at nodes. Using the data at these nodes, one can fit an appropriate function through an overdetermined system of linear equations which has more equations (m) than unknowns (n), i.e., the coefficient matrix has more rows than columns ($m > n$). In this case, a solution can be found by requiring that the magnitude of the residual vector r, defined by $r = Ax - b$ be minimized. The simplest and most frequently used measure of the magnitude of $\mathbf{r}$ is the Euclidean length, $\mathbf{r}^T\mathbf{r}$. This approach leads to the least squares solution of the overdetermined system.

$$\mathbf{r}^T\mathbf{r} = (\mathbf{x}^T\mathbf{A}^T - \mathbf{b}^T)(\mathbf{A}\mathbf{x} - \mathbf{b}) \tag{6.27}$$

$$\mathbf{r}^T\mathbf{r} = \mathbf{x}^T\mathbf{A}^T\mathbf{A}\mathbf{x} - \mathbf{x}^T\mathbf{A}^T\mathbf{b} - \mathbf{b}^T\mathbf{A}\mathbf{x} + \mathbf{b}^T\mathbf{x} \tag{6.28}$$

Above is a quadratic equation, that means it is a convex function. Then, one can take derivative to find the minimum;

$$0 = \mathbf{A}^T\mathbf{A}\mathbf{x} - \mathbf{A}^T\mathbf{b} \rightarrow \mathbf{A}^T\mathbf{A}\mathbf{x} = \mathbf{A}^T\mathbf{b} \rightarrow \mathbf{C}\mathbf{x} = \mathbf{d} \tag{6.29}$$

$$\mathbf{x} = \mathbf{C}^{-1}\mathbf{d} \tag{6.30}$$

$$F_1 = k_1 + (x_1)k_2 + (x_1)^2 k_3 + \cdots + (x_1)^{m-1} k_m$$

$$F_2 = k_1 + (x_2)k_2 + (x_2)^2 k_3 + \cdots + (x_2)^{m-1} k_m$$

$$F_3 = k_1 + (x_3)k_2 + (x_3)^2 k_3 + \cdots + (x_3)^{m-1} k_m \tag{6.31}$$

$$\vdots$$

$$F_n = k_1 + (x_n)k_2 + (x_n)^2 k_3 + \cdots + (x_n)^{m-1} k_m$$

$$r_1 = k_1 + (x_1)k_2 + (x_1)^2 k_3 + \cdots + (x_1)^{m-1} k_m - F_1$$

$$r_2 = k_1 + (x_2)k_2 + (x_2)^2 k_3 + \cdots + (x_2)^{m-1} k_m - F_2$$

$$r_3 = k_1 + (x_3)k_2 + (x_3)^2 k_3 + \cdots + (x_3)^{m-1} k_m - F_3 \tag{6.32}$$

$$\vdots$$

$$r_n = k_1 + (x_n)k_2 + (x_n)^2 k_3 + \cdots + (x_n)^{m-1} k_m - F_n$$

$$
\begin{bmatrix} F_1 \\ F_2 \\ F_3 \\ \vdots \\ F_n \end{bmatrix}
=
\begin{bmatrix}
1 & x_1 & x_1^2 & \cdots & (x_1)^{m-1} \\
1 & x_2 & x_2^2 & \cdots & (x_2)^{m-1} \\
1 & x_3 & x_3^2 & \cdots & (x_3)^{m-1} \\
\vdots & \vdots & \vdots & \vdots & \vdots \\
1 & x_n & x_n^2 & \cdots & (x_n)^{m-1}
\end{bmatrix}
\begin{bmatrix} k_1 \\ k_2 \\ k_3 \\ \vdots \\ k_m \end{bmatrix}
\tag{6.33}
$$

$$
\begin{bmatrix}
1 & 1 & 1 & \cdots & 1 \\
x_1 & x_2 & x_3 & \cdots & x_n \\
x_1^2 & x_2^2 & x_3^2 & \cdots & x_n^2 \\
\vdots & \vdots & \vdots & \cdots & \vdots \\
(x_1)^{m-1} & (x_2)^{m-1} & (x_3)^{m-1} & \cdots & (x_n)^{m-1}
\end{bmatrix}
\begin{bmatrix} F_1 \\ F_2 \\ F_3 \\ \vdots \\ F_n \end{bmatrix}
=
$$

$$\begin{bmatrix} 1 & 1 & 1 & \cdots & 1 \\ x_1 & x_2 & x_3 & \cdots & x_n \\ x_1{}^2 & x_2{}^2 & x_3{}^2 & \cdots & x_n{}^2 \\ \vdots & \vdots & \vdots & \cdots & \vdots \\ (x_1)^{m-1} & (x_2)^{m-1} & (x_3)^{m-1} & \cdots & (x_n)^{m-1} \end{bmatrix} \begin{bmatrix} 1 & x_1 & x_1{}^2 & \cdots & (x_1)^{m-1} \\ 1 & x_2 & x_2{}^2 & \cdots & (x_2)^{m-1} \\ 1 & x_3 & x_3{}^2 & \cdots & (x_3)^{m-1} \\ \vdots & \vdots & \vdots & \vdots & \vdots \\ 1 & x_n & x_n{}^2 & \cdots & (x_n)^{m-1} \end{bmatrix} \begin{bmatrix} k_1 \\ k_2 \\ k_3 \\ \vdots \\ k_m \end{bmatrix} \quad (6.34)$$

After doing the algebra, the displacement of the beam will found by the polynomial of $-1.133x^8 + 4.836x^7 - 5.436x^6 - 4.355x^5 + 14.72x^4 - 12.29x^3 + 3.732x^2 - 0.1418x + 0.1221$. The comparison of the fitted and finite element displacement data is depicted in Figure 6.3.
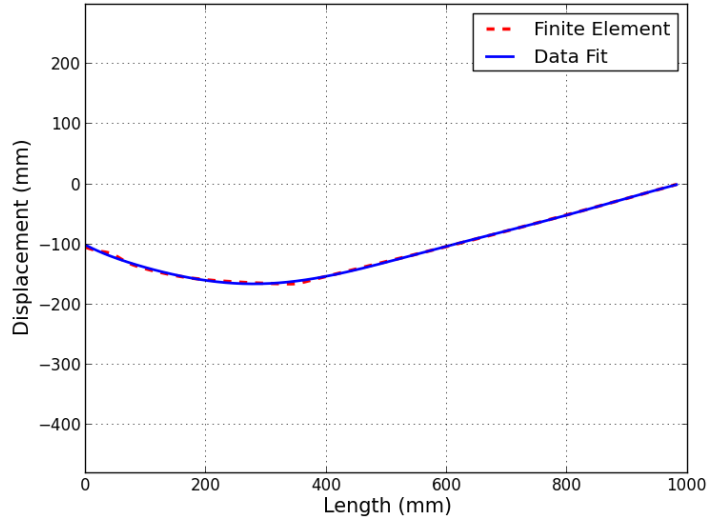
Figure 6.3. The comparison of displacement results of linear least squares and the finite element.

By using the Eq 6.2, the energy value will be 21356.6 J. However, according to the finite element results, the beam has accumulated 3389.8 J. By equating the two energies, one can find the effective Young's modulus by $70\dfrac{3389.8}{21356.6} = 11.11$ GPa.

After the calculation of effective Young's modulus, the deformation of the beam can be found by assuming the loading to be 41491.6 N/m. The comparison of the analytical model and the data by the finite element analysis is depicted in Figure 6.4.

Noting that the calculation made here is only valid for EuroNCAP offset frontal impact conditions. For other test, the stiffness of the spring and effective Young's modulus need to be calculated.
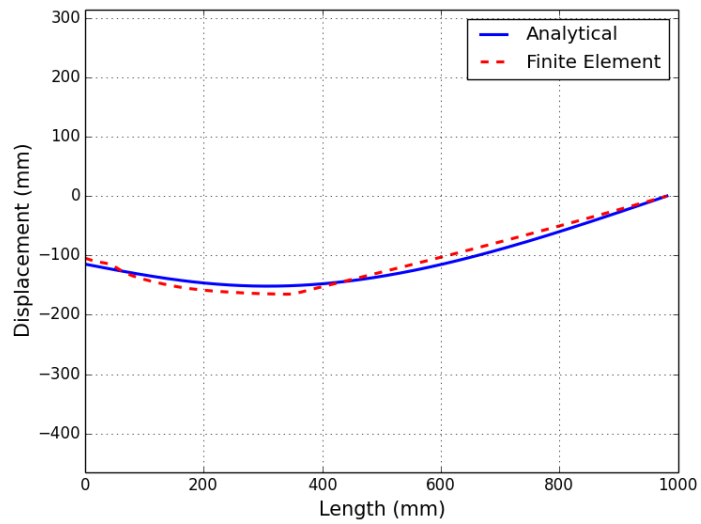
Figure 6.4. The comparison displacement results of analytical model and the finite element.

7. CONCLUSION

In this thesis, the bumper-beam and the crash-box of a vehicle are optimized for crashworthiness.

In the bumper-beam study, the shape of a bumper beam is optimized under impact conditions very similar to EuroNCAP tests to maximize its crashworthiness. The coordinates of the key points used to define the spline curves representing the cross-sectional profile are taken as the optimization variables. The deformable barrier used in the standard tests is modeled as rigid. In order to account for the energy absorbed by the deformable barrier, a correction factor is calculated for the mass of the vehicle. The bumper-beam and crash-boxes are modeled as deformable bodies in full detail. In order to reduce the computational time, a lumped-parameter model is developed to mimic the behavior of the main vehicle body using a parametric system identification method. The parameters of the lumped-parameter car model are tuned to reflect the response of the car predicted by the full car model. The resulting optimum shape found by the optimization algorithm depends highly on the formulation of the objective function, the number of variables, and the range of the feasible domain. By choosing different values for the weighting factors of the terms in the objective function, different optimal shapes are obtained. The two optimum shapes obtained in this study show significant improvement over the one currently in-use; specific strain energy absorbed by the optimal beam is larger by 15%. The resistance to crash at low speeds is also significantly improved. From the manufacturing point of view, the new shape of the bumper-beam does not bring additional cost due to the fact that one can extrude the profile just like the one currently-in-use.

In the crash-box study, the shape of a crash-box is optimized under impact conditions very similar to EuroNCAP tests to maximize its crashworthiness. The parameters defining the shapes of the cross-sectional and longitudinal profiles as well as the thickness are taken as the optimization variables. The crash-box is modeled as a deformable body in full detail. On the other hand, a lumped-parameter model is developed to ac-

count for the structural response of the bumper-beam and the main body of the car. The optimum shapes obtained in this study show significant improvement over the circular benchmark design. By choosing different values for the weighting factors of the terms in the objective function, different optimal shapes are obtained. The best results are obtained, if only the first term, which is specific energy absorption, and the third term, which is the maximum force and its jerk effect, in the objective function are considered. When the thickness is allowed to vary, the crashworthiness of the crash-box is improved.

It is possible to reach similar results using analytical approach by making use of the finite element results. But this strategy needs calculating the effective Young's modulus and the stiffness of the spring for the crash-box, which makes the approximation valid only for the case for which finite element results are obtained. As a future study, the analytical model can be developed by using a constitutive model that accounts for plastic deformation at large strain.

The designs optimized for maximum crashworthiness at high-velocity impact may not satisfy low-velocity requirements; but it is possible to find near global optimum designs that show satisfactory performance for low-velocity impacts. Furthermore, increasing the crashworthiness of a certain part may not lead to an increase in the performance of the system's general behavior. However, in this study, the assembly of the optimal designs for the bumper-beam and the crash-box outperforms the currently-in-use design as the results indicate. The optimal designs found using rigid barrier would be similar to the ones with deformable barrier if not the same. To close this gap, if there is any, the optimal shapes found can be further subjected to change under fully modeled car and barrier structure with a local optimizer as a future study.

In the present study, a methodology is developed to find the globally optimum shapes of vehicle parts for maximum crashworthiness. The number of design variables and the range of values they may take are taken to be large and also a global optimizer is used. Further, the future study will be to consider all the parts having significant effect on the crashworthiness of the vehicle and optimize their overall response starting

from their optimum shapes. Besides, in this study, the design spaces are selected based on the benchmark shapes in order to compare the results with the benchmarks. However, the range of the design variables can be taken to be larger to reach much better results.

REFERENCES

1. Kokkula, S., O. S. Hopperstad, O. G. Lademo and T. Berstad, "Offset Impact Behaviour of Bumper Beam-Longitudinal Systems: Numerical Simulations", *International Journal of Crash*, Vol. 11, No. 4, pp. 317–336, 2006.

2. Kokkula, S., M. Langseth, O. S. Hopperstad and O. Lademo, "Offset Impact Behaviour of Bumper Beam-Longitudinal Systems: Experimental Investigations", *International Journal of Crash*, Vol. 11, No. 4, pp. 299–316, 2006.

3. Liu, Y. and M. L. Day, "Experimantal Analysis and Computer Simulation of Automotive Bumper System under Impact Conditions", *International Journal for Computational Methods in Engineering Science and Mechanics*, Vol. 9, pp. 51–59, 2008.

4. Marzbanrad, J., M. Alijanpour and M. S.Kiasat, "Design and Analysis of an Automotive Bumper Beam in Low-Speed Frontal Crashes", *Thin-Walled Structures*, Vol. 47, pp. 902–911, 2009.

5. Patel, N. M., C. L. Penninger and J. E. Renaud, "Topology Synthesis of Extrusion-Based Nonlinear Transient Designs", *Journal of Mechanical Design*, Vol. 191, pp. 1–11, 2009.

6. Farkas, L., C. Canadas, S. Donders, T. van Langenhove and N. Tzannetakis, "Optimization Study of a Parametric Vehicle Bumper Subsystem Under Multiple Load Cases Using Lms Virtual Lab and Optimus", *7th European LS-DYNA Conference*, 2009.

7. Farkas, L., D. Moens, S. Donders and D. Vandepitte, "Optimisation Study of a Vehicle Bumper Subsystem with Fuzzy Parameters", *Mechanical Systems and Signal Processing*, Vol. 32, pp. 59–68, 2012.

8. Duponcheele, G. and D. G. Tilley, "Topological Optimization of a Bumper Beam

via the Messy Genetic Algorithm", *Proceedings of the Institution of Mechanical Engineers*, 1998.

9. Zhang, Z., S. Liu and Z. Tang, "Design Optimization of Cross-Sectional Configuration of Rib-Reinforced Thin-Walled Beam", *Thin-Walled Structures*, Vol. 47, pp. 868–878, 2009.

10. Zarei, H. and M. Kröger, "Bending Behavior of Empty and Foam-Filled Beams: Structural Optimization", *International Journal of Impact Engineering*, Vol. 35, pp. 521–529, 2008.

11. Shin, M., S. I. Yi and G. J. Park, "Structural Optimization of the Automobile Frontal Structure for Pedestrian Protection and the Low-Speed Impact Test", *Journal of Automobile Engineering*, Vol. 222, pp. 2373–2387, 2008.

12. Mullerschon, H., N. Lazarov and K. Witowski, "Application of Topology Optimization for Crash with LS OPT/Topology", *11th International LS DYNA Users Conference*, 2010.

13. Kim, S., K. W. Lee, D. H. Lee and H. G. Lee, "Bumper System Development to Meet New IIHS Bumper Test Using CAE and Optimization", *SAE World Congress & Exhibition*, 2009.

14. Detwiler, D. T. and R. A. Miller, "Development of a Sport Utility Front Bumper System for Pedestrian Safety and 5 mph Impact Performance", *Honda R&D Americas Paper Number 01-S6-W-145*.

15. Lee, J.-W., K.-H. Yoon, Y.-S. Kang and G.-J. Park, "Vehicle Hood and Bumper Structure Design to Mitigate Casualties of Pedestrian Accidents", *SAE Paper Number 05-0105*.

16. Park, D. K. and C. D. Jang, "Optimum SUV Bumper System Design considering Pedestrian Performance", *International Journal of Automotive Technology*, Vol.

11/ 6, pp. 819–824, 2010.

17. Davoodi, M., S. Sapuan and R. Yunus, "Conceptual Design of a Polymer Composite Automotive Bumper Energy Absorber", *Materials and Design*, Vol. 29, pp. 1447–1452, 2008.

18. Yamazaki, K. and J. Han, "Maximization of the Crushing Energy Absorption of Tubes", *Structural Optimization*, Vol. 16, pp. 37–46, 1998.

19. Lee, S.-H., H.-Y. Kim and S.-I. Oh, "Cylindrical Tube Optimization using Response Surface Method Based on Stochastic Process", *Journal of Materials Processing Technology*, Vol. 130-131, pp. 490–496, 2002.

20. Sheriff, N. M., N. Gupta, R. Velmurugan and N. Shanmugapriyan, "Optimization of Thin Conical Frusta for Impact Energy Absorption", *Thin-Walled Structures*, Vol. 46, pp. 653–666, 2008.

21. Avalle, M. and G. Chiandussi, "Optimisation of a Vehicle Energy Absorbing Steel Component with Experimental Validation", *International Journal of Impact Engineering*, Vol. 34, pp. 843–858, 2007.

22. Hou, S., Q. Li, S. Long, X. Yang and W. Li, "Multiobjective Optimization of Multi-Cell Sections for the Crashworthiness Design", *International Journal of Impact Engineering*, Vol. 35, pp. 1355–1367, 2008.

23. Hou, S., Q. Li, S. Long, X. Yang and W. Li, "Design Optimization of Regular Hexagonal Thin-Walled Columns with Crashworthiness Criteria", *Finite Elements in Analysis and Design*, Vol. 43, pp. 555 – 565, 2007.

24. Lönn, D., O. Fyllingen and L. Nilssona, "An Approach to Robust Optimization of Impact Problems using Random Samples and Meta-modelling", *International Journal of Impact Engineering*, Vol. 37, pp. 723–734, 2010.

25. Acar, E., M. Guler, B. Gerceker, M. Cerit and B. Bayram, "Multi-Objective Crash-

worthiness Optimization of Tapered Thin-Walled Tubes with Axisymmetric Indentations", *Thin-Walled Structures*, Vol. 49, No. 1, pp. 94–105, 2011.

26. Qi, C., S.Yang and F. Dong, "Crushing Analysis and Multiobjective Crashworthiness Optimization of Tapered Square Tube under Oblique Impact Loading", *Thin-Walled Structures*, Vol. 59, pp. 103–119, 2012.

27. Liu, Y., "Optimum Design of Straight Thin-Walled Box Section Beams for Crashworthiness Analysis", *Finite Elements in Analysis and Design*, Vol. 44, pp. 139–147, 2008.

28. Liu, Y., "Crashworthiness Design of Multi-Corner Thin-Walled columns", *Thin-Walled Structures*, Vol. 46, pp. 1329–1337, 2008.

29. Y., S. and C. Qi, "Multiobjective Optimization for Empty and Foam-Filled Square Columns under Oblique Impact Loading", *International Journal of Impact Engineering*, Vol. 54, pp. 177–191, 2013.

30. Zarei, H. and M. Kröger, "Multiobjective Crashworthiness Optimization of Circular Aluminum Tubes", *Thin-walled Structures*, Vol. 44, pp. 301–308, 2006.

31. Kim, C. and J. S. Arora, "Development of Simplified Dynamic Models using Optimization: Application to Crushed Tubes", *Comput. Methods Appl. Mech. Engrg.*, Vol. 192, pp. 2073–2097, 2003.

32. Santosa, S. and T. Wierzbicki, "Crash Behavior of Box Columns Filled with Aluminum Honeycomb or Foam", *Computers and Structures*, Vol. 68, pp. 343–367, 1998.

33. Zarei, H. and M. Kröger, "Optimum Honeycomb Filled Crash Absorber Design", *Materials and Design*, Vol. 29, pp. 193–204, 2008.

34. Zarei, H. and M. Kröger, "Optimization of the Foam-Filled Aluminum Tubes for Crush Box Application", *Thin-Walled Structures*, Vol. 46, pp. 214–221, 2008.

35. Hanssen, A., M. Langseth and O. Hopperstad, "Optimum Design for Energy Absorption of Square Aluminium Columns with Aluminium Foam Filler", *International Journal of Mechanical Sciences*, Vol. 43, pp. 153–176, 2001.

36. Ahmad, Z. and D. Thambiratnam, "Dynamic Computer Simulation and Energy Absorption of Foam-Filled Conical Tubes under Axial Impact Loading", *Computers and Structures*, Vol. 87, pp. 186–197, 2009.

37. Sun, G., G. Li, S. Hou, S. Zhou, W. Li and Q. Li, "Crashworthiness Design for Functionally Graded Foam-Filled Thin-Walled Structures", *Materials Science and Engineering A*, Vol. 527, pp. 1911–1919, 2010.

38. Yin, H., G. Wen, S. Hou and K. Chen, "Crushing Analysis And Multiobjective Crashworthiness Optimization Of Honeycomb-Filled Single And Bitubular Polygonal Tubes", *Materials and Design*, Vol. 32, pp. 4449–4460, 2011.

39. Bi, J., H. Fang, Q. Wang and X. Ren, "Modeling and Optimization of Foam-Filled Thin-Walled Columns for Crashworthiness Designs", *Finite Elements in Analysis and Design*, Vol. 46, pp. 698–709, 2010.

40. F.Tarlochan, F.Samer, A.M.S.Hamouda and K. K. S.Ramesh and, "Design of Thin Wall Structures for Energy Absorption Applications: Enhancement of Crashworthiness due to Axial and Oblique Impact Forces", *Thin-WalledStructures*, Vol. 71, pp. 7–17, 2013.

41. Witteman, W. J., "Improved Vehicle Crashworthiness Design by Control of the Energy Absorption for Different Collision Situations", *Technische Universiteit Eindhoven*, 1999.

42. "Frontal Impact", 2014, http://www.euroncap.com/tests/frontimpact.aspx, [Accessed 11.2014].

43. Deb, A., A. Naravane and E. C. Chirwa, "An Offset Rigid Barrier-Based Test:

Equivalence to the Insurance Institute for Highway Safety Frontal Offset Impact Safety Test", *International Journal of Crashworthiness*, Vol. 11, No. 4, pp. 281 – 290, 2006.

44. Liao, X., Q. Li, X. Yang, W. Zhang and W. Li, "Multiobjective Optimization for Crash Safety Design of Vehicles using Stepwise Regression Model", *Structural and Multidisciplinary Optimization*, Vol. 35, pp. 561–569, 2008.

45. Jonsen, P., E. Isaksson, K. Sundin and M. Oldenburg, "Identification of Lumped Parameter Automotive Crash Models for Bumper System Development", *International Journal of Crashworthiness*, Vol. 14, No. 6, pp. 533–541, 2009.

46. Pawlus, W., H. Reza and K. G. Robbersmyr, "Application of Viscoelastic Hybrid Models to Vehicle Crash Simulation", *International Journal of Crashworthiness*, Vol. 16, No.2, pp. 195–205, 2011.

47. Karimi, H. R., W. Pawlus and K. G.Robbersmyr, "Signal Reconstruction, Modeling and Simulation of a Vehicle Full-Scale Crash Test Based on Morlet Wavelets", *Neurocomputing*, Vol. 93, pp. 88–99, 2012.

48. Marler, R. T., C.-H. Kim and J. S. Arora, "System Identification of Simplified Crash Models using Multi-Objective Optimization", *Comput. Methods Appl. Mech. Engrg.*, Vol. 195, pp. 4383–4395, 2006.

49. Fang, H., K. Solanki and M. F. Horstemeyer, "Numerical Simulations of Multiple Vehicle Crashes and Multidisciplinary Crashworthiness Optimization", *International Journal of Crashworthiness*, Vol. 10, No. 2, pp. 161–171, 2010.

50. "Finite Element Model Archive", 2014, http://www.ncac.gwu.edu/vml/models.html, [Accessed 01.2014].

51. Tanlak, N., F. Sonmez and E. Talay, "Detailed and Simplified Models of Bolted Joints under Impact Loading.", *The Journal of Strain Analysis for Engineering*

Design, Vol. 46, No. 3, pp. 213–225, 2011.

52. Johnson, G. R. and W. H. Cook, "A Constitutive Model and Data for Metals Subjected to Large Strains, High Strain Rates, and High Temperatures", *Proceedings of the 7th International Symposium Ballistics*, 1983.

53. Lesuer, D., G. Kay and M. LeBlanc, "Modeling Large Strain, High Rate Deformation in Metals", *Modeling the performance of engineering structural materials II. In Proceedings of a symposium sponsored by the SMD of TMS, Indianapolis, IN, p. 75-86.*, 2001.

54. Corbett, B. M., *Hypervelocity Impact Damage Response and Characterization of Thin Plate Targets at Elevated Temperatures*, Ph.D. Thesis, University of Denver, 2008.

55. Johnson, G. R. and W. H. Cook, "Fracture Characteristics of Three Metals Subjected to Various Strains, Strain Sates, Temperatures and Pressures", *Engineering Fracture Mechanics*, Vol. 21, No. 1, pp. 31–48, 1985.

56. *ABAQUS Analysis User's Manual*, ABAQUS, Inc., Providence, 2004.

57. Liuwei, G. and Y. Jilin, "Dynamic Bending Response of Double Cylindrical Tubes Filled with Aluminum Foam", *International Journal of Impact Engineering*, Vol. 38, pp. 85–94, 2011.